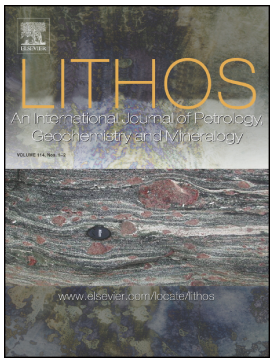

Shoshonitic enclaves in the high Sr/Y Nyemo pluton, southern Tibet: Implications for Oligocene magma mixing and the onset of extension of the southern Lhasa terrane

Zhenzhen Wang, Zhidan Zhao, Paul D. Asimow, Dong Liu, Di-Cheng Zhu, Xuanxue Mo, Qing Wang, Liangliang Zhang, Lawangin Sheikh

PII: S0024-4937(20)30127-4

DOI: https://doi.org/10.1016/j.lithos.2020.105490

Reference: LITHOS 105490

To appear in: *LITHOS*

Received date: 4 December 2019

Revised date: 17 March 2020

Accepted date: 18 March 2020

Please cite this article as: Z. Wang, Z. Zhao, P.D. Asimow, et al., Shoshonitic enclaves in the high Sr/Y Nyemo pluton, southern Tibet: Implications for Oligocene magma mixing and the onset of extension of the southern Lhasa terrane, *LITHOS* (2020), https://doi.org/10.1016/j.lithos.2020.105490

Shoshonitic enclaves in the high Sr/Y Nyemo pluton, southern Tibet: Implications for Oligocene magma mixing and the onset of extension of the southern Lhasa terrane

Zhenzhen Wang[a], Zhidan Zhao[a,] *, Paul D. Asimow[b], Dong Liu[a], Di-Cheng Zhu[a] Xuanxue Mo[a], Qing Wang[a], Liangliang Zhang[a], Lawangin Sheikh[a]

a. State Key Laboratory of Geological Processes and Mineral Resources, and School of Earth Science and Resources, China University of Geosciences, Beijing 100083, China

b. Division of Geological and Planetary Sciences, California Institute of Technology, Pasadena, CA 91125, USA

Manuscript submitted to Lithos

*Corresponding author at:

29 Xueyuan Road, Haidian District, Beijing 100083, China.

Fax: (+86-10) 8232-1115; Telephone: (+86) 1368-111-8299

E-mail: zdzhao@cugb.edu.cn

Abstract

Post-collisional potassic and high Sr/Y magmatism in the Lhasa terrane provides critical constraints on the timing and mechanism of subduction of Indian lithosphere and its role in the uplift of the Tibetan Plateau. Here, we report whole-rock geochemistry, mineral geochemistry, zircon U-Pb ages, and in situ zircon Hf isotope ratios for the Nyemo pluton, a representative example of such magmatism. The Nyemo pluton is composed of high Sr/Y host rocks and coeval shoshonitic mafic microgranular enclaves (MMEs). Whole-rock compositions of the host rocks and MMEs form linear trends in Harker diagrams, consistent with modification of both end-members by magma mixing. Although the main high Sr/Y phase of the pluton formed by partial melting of the lower crust of the thickened Lhasa terrane, the MMEs display abnormally enriched light rare earth elements, low whole-rock $\varepsilon_{Nd}(t)$ and low zircon $\varepsilon_{Hf}(t)$ that suggest derivation from low degree melting of hydrous and enriched mantle. Based on the occurrence of shoshonitic magma and high La/Yb and high Sr/Y with adakitic affinity host rocks around 30Ma, the Nyemo pluton is best explained as a record of onset of extension that resulted from convective removal of the mantle lithosphere beneath Tibet in the Oligocene.

Keywords: high Sr/Y rocks, shoshonitic MMEs, magma mixing, convective removal, extension onset, Lhasa terrane, Tibetan plateau

1. Introduction

Shoshonitic rocks, enriched in large ion large ion lithophile elements (LILEs) and light rare earth elements (LREEs), with high K_2O/Na_2O, is characteristically appearing in orogenic environments. Although, numerous studies focused on the shoshonitic rocks, the magmatic origin of shoshonitic rocks is still controversial. Some have argued that shoshonitic magma originate from dehydration melting of enriched metabasaltic amphibolite at the base of the crust (Ye-Piper et al., 2009). Most authors, though, have proposed that shoshonitic rocks are derived from low-degree melts of hydrous and enriched mantle (Zhao et al., 2009).

After continental collision between India and Eurasia, extensive post-collisional potassic-rich (shoshonitic) rocks were emplaced along a series of N–S-trending rifts (Gao et al. 2007), but their petrogenesis and geodynamic processes remain debated. Some scholars suggested that they are derived from convective removal of the lower part of previously thickened lithospheric mantle (Zhao et al., 2009). Alternative hypotheses, however, include (a) linked to intracontinental subduction of Indian continental lithosphere (Ding et al., 2003); (b) resulted from break-off of a northward subducted slab of Indian continental lithosphere (Zhang et al., 2014).

It is noteworthy that previous researches on post-collisional shoshonitic rocks were mainly focused in Miocene, between 25 and 8 Ma (Zhao et al.,2009), whereas Oligocene shoshonitic magmatism in southern Lhasa terrane was rarely reported. Recently, we have identified Oligocene shoshonitic rocks exposed as mafic enclaves, entrained by high Sr/Y pluton in southern Lhasa terrane. On account of the occurrence of post-collisional shoshonitic magmatism may be the signal of extension onset and provide a critical constraint on the mechanism of lithospheric extension of the southern Tibetan Plateau, and the post-collisional high Sr/Y with adakitic affinity

units may provide constraint on the timing and mechanism of the uplift of the Tibetan Plateau (Hou et al., 2004), it is important to understand the origin, evolution and genetic relationship of Oligocene shoshonitic enclaves with their high Sr/Y host rocks.

In this paper, we present whole-rock major and trace element compositions, mineral chemical analysis, zircon U-Pb ages, zircon Hf isotope ratios, and whole-rock Sr-Nd-Pb isotopic data for newly discovered Oligocene Nyemo pluton of the southern Lhasa terrane. Together with previously published data, we have focused on the Oligocene shoshonitic mafic enclaves and their high Sr/Y host rocks of Nyemo pluton in order to understand their genetic mechanism, to evaluate the nature of their magma source, and to determine the nature of the relationship between the magmatism and the subduction of the Indian plate.

2. Geological setting and sample description

The Tibetan Plateau, part of the Eastern Tethyan tectonic domain, was assembled through a series of terrane collisions culminating in the India-Asia collision and large-scale orogenic uplift. From north to south, Tibet is divided into three major E-W trending belts: the Songpan-Ganze complex, the Qiangtang terrane, and the Lhasa terrane (Fig. 1a). The Lhasa terrane, bounded on the north by the Banggong-Nujiang suture zone (BNS) (Yin and Harrison, 2000; Zhu et al., 2011), locally defines the southernmost margin of the Eurasian continent and is separated from Indian crust by the Indus-Yarlung Zangbo suture (IYZS). Furthermore, the Lhasa terrane can be subdivided by the Shiquan River–Nam Tso mélange zone (SNMZ) and the Luobadui–Milashan fault (LMF) (Zhu et al., 2011) into the northern, central, and southern Lhasa subterranes, respectively (Fig. 1b). The west Nyainqentanglha Group, and the northeast Amdo gneiss are thought to represent the ancient basement of Lhasa terrane. Sedimentary strata in southern subterrane includes the Ordovician metamorphic

clastic rocks and carbonate formation, the Jurassic Yeba formation, the Jurassic-Cretaceous Sangri group, and the Cretaceous limestone-clastic sequence (Wei et al., 2017).

Owing to the prolonged subduction of Neo-Tethys and subsequent India-Eurasia continental collision, the southern Lhasa terrane has been the focus of voluminous Mesozoic-Cenozoic magmatism (Ji et al., 2009; Zhu et al., 2011). Previous studies have recognized four magmatic episodes: (1) a Jurassic suite (205-152 Ma), mainly granodiorite, tonalite, and andesite (Zhu et al., 2008); (2) Cretaceous (109-80 Ma) activity resulting from the northward subduction of Neo-Tethys, predominantly gabbro, diorite, granodiorite and granite (Ma et al., 2013); (3) Paleocene-Eocene (65-41 Ma) activity recording the large-scale collision between India and Eurasian and Neo-Tethyan slab break-off, including granitoids and the Linzizong Formation volcanic arc (Ji et al., 2009); and (4) post-collisional Oligocene-Miocene (30-10 Ma) magmatism, including high Sr/Y rocks, potassic-ultrapotassic volcanic rocks and peraluminous granites (Chung et al., 2009; Zhao et al., 2009; Chu et al., 2011).

The most recent, post-collisional, episode is well-exposed in the central and southern Lhasa terrane. Ultrapotassic rocks (24-10 Ma) are thought to be derived from metasomatized mantle are mainly found in the central Lhasa subterrane (Zhao et al., 2009; Liu et al., 2017). Potassic volcanic rocks occur in both the central and southern subterranes (Guo et al., 2013). In contrast, the high Sr/Y plutonic rocks are mainly found in the southern Lhasa subterrane, with ages from 31 to 9 Ma. They form a series of small-volume intrusions or veins that mainly intrude the Gangdese pluton or Cenozoic volcanic rock series (Chung et al., 2009; Ji et al., 2009; Chu et al., 2011, Liu et al., 2017).

This study focuses on the petrogenesis and geodynamic implication of the

Nyemo pluton in southern Tibet. It intrudes country rocks ranging in age from the Jurassic volcanic strata of the Sangri group to an Eocene gabbroic diorite (Fig. 1c). The Nyemo pluton consists mainly of quartz monzonite and granodiorite that host abundant MMEs (Fig. 2a). The host rocks are light gray with granitic texture and are mainly composed of K-feldspar, plagioclase, biotite, and quartz with minor apatite, titanite, zircon and magnetite as accessory minerals. The MMEs are dioritic, composed of plagioclase, K-feldspar, biotite, amphibole and quartz, with accessory apatite, zircon, titanite (Figs. 2a-e).

3. Analytical methods

3.1 Zircon U-Pb dating and Hf isotopes

Zircons were extracted from crushed and sieved samples using heavy liquid separation, hand-picked and mounted in epoxy resin, and polished to expose interiors for calthodoluminescence (CL) and reflected light imaging. The zircon U-Pb dating was conducted using the LA-ICP-MS at the laboratory of Ocean Lithosphere and Mantle Dynamics (OLMD), Institute of Oceanology, Chinese Academy of Sciences and at the Milla Laboratory, Institute of Earth Sciences, China University of Geosciences, Beijing. Both labs use ablation diameter of 35 μm and an 8 Hz repetition rate. The external standard for U-Pb dating was zircon standard 91500 (Wiedenbeck et al., 1995). Details of instrumental operating conditions and methods of off-line data processing are documented in Liu et al. (2010).

Zircon Hf isotope analysis was conducted in situ on the same mounts using a Thermo-Finnigan Neptune MC-ICPMS equipped with a 193 nm excimer laser-ablation system at the Institute of Geology and Geophysics, Chinese Academy of Sciences (IGGCAS). The laser beam spot diameter was 60-65 μm and both 4 Hz

and 8 Hz pulse frequencies were used. Mud Tank and GJ-1 zircons were analyzed as quality control standards. The average $^{176}Hf/^{177}Hf$ for zircon standard 91500 was 0.282303±0.000021 (2SD, n=52), in agreement with the recommended value (Woodhead et al., 1998).

3.2 Mineral geochemistry

Backscattered electron (BSE) images and major element analyses of minerals were collected using the JEOL JXA-8200 five-spectrometer electron microprobe in the Division of Geological and Planetary Sciences at the California Institute of Technology. Analytical conditions were 15 kV and 25 nA with a 10 μm beam diameter and counting times of 30 seconds on-peak. Standards include synthetic forsterite (Mg), fayalite (Fe), Mn-olivine (Mn), anorthite (Ca, Si, and Al), TiO_2 (Ti), Cr_2O_3 (Cr) and natural Amelia albite (Na) and Asbestos microcline (K). Synthetic MgO and Al_2O_3 standards were also analyzed and the mean atomic number background correction routine was used, calibrated with all standards that do not contain an element of interest. The CITZAF matrix correction procedure was used (Armstrong, 1995). Detection limits (wt.%) are 0.05 Si, 0.04 Ti, 0.06 Al, 0.06 Fe, 0.02 Mg, 0.02 Ca, 0.03 Na, 0.02 K, 0.05 Cr, and 0.06 Mn.

3.3 Whole-rock major and trace elements

Whole-rock major and trace element analyses were carried out at the Wuhan Sample Solution Analytical Technology Technology Co., Ltd., Wuhan, China. The major elements conducted by X-ray fluorescence (Rigaku Primus II) at the Wuhan Sample Solution Analytical Technology Co., Ltd., Wuhan, China. Sample powders were dried to remove adsorbed water, weighed, heated for 1 hour at 1050 °C to oxidize and measure loss on ignition, and mixed with twice their weight in Li-borate

flux. The mixtures were melted and quenched to produce glass discs for analysis. The trace element analyses were conducted by solution ICP-MS (Agilent 7700e). The detailed sample digestion procedure and the resulting analytical precision and accuracy are referred to Liu et al. (2008) and summarized in the methods.

3.4 Whole-rock Sr-Nd-Pb isotopes

The whole rock isotope ratios of Sr, Nd, and Pb were conducted on a Thermo-Finnigan Neptune MC-ICPMS at the Isotope Geochemistry and Geochronology Research Center, Carleton University (IGGRC-CU), Ottawa, Canada. The measured $^{143}Nd/^{144}Nd$ ratios for the samples were corrected for offsets of the measured JNdi-1 standard against a reference value of 0.512115 (Tanaka et al, 2000). Pb isotope ratios were corrected for offsets of measured NBS981 standard against the reference values of Todt et al. (1996). Standards BCR-2 and NBS987 yield average $^{87}Sr/^{86}Sr$ ratios of 0.705019 (n=3) and 0.710258±0.000025 (2σ, n=13), respectively, while the average $^{143}Nd/^{144}Nd$ ratios of BCR-2 and international standard JNdi-1 are 0.512640±0.000008 (n=1) and 0.512088±0.000013 (2σ, n=18), respectively. NBS981 yielded average ratios of $^{206}Pb/^{204}Pb$=16.9317±0.0012 (2σ, n=16), $^{207}Pb/^{204}Pb$ = 15.4853 ± 0.11 (2σ, n=16), and $^{208}Pb/^{204}Pb$ = 36.6784 ± 0.0035 (2σ, n=16). BCR-2 yields $^{206}Pb/^{204}Pb$ = 18.7579, $^{207}Pb/^{204}Pb$ = 15.6173, and $^{208}Pb/^{204}Pb$ = 38.7226. The total procedural blanks at IGGRC-CU are <100, <250 and <50 pg for Pb, Sr and Nd respectively.

4. Results

4.1 Zircon geochronology and Hf isotopes

Zircon U-Pb dating results are given in Table S1.

Four samples (15TNM10-1; 15TNM10-2; NM1716; NM1717) of the Nyemo

pluton were selected for zircon U-Pb dating (Fig. 3). All the zircon grains are colorless and euhedral, with elongation rations ranging from 1:1 to 3:1, showing clear oscillatory zoning in CL images and high Th/U (0.29-2.02).

Zircons from the host quartz monzonite samples (15TNM10-1, NM1717) yield weighted mean $^{206}Pb/^{238}U$ ages of 29.5 ± 0.2 Ma (2σ, n=16) and 27.5 ± 0.2 Ma (2σ, n=14). Similarly, zircons separated from MME samples (15TNM10-2, NM1716) yield weighted mean $^{206}Pb/^{238}U$ ages of 29.0 ± 0.3 Ma (2σ, n=11) and 27.8 ± 0.2 Ma (2σ, n=14).

Zircons from one host rock sample (15TNM10-1) and one MME sample (15TNM10-2) were selected for *in situ* Hf isotope analysis (Table S2). Both samples display heterogeneous Hf isotopic ratios in their zircon populations (Fig. 4). Sample 15TNM10-1 zircons have $^{176}Hf/^{177}Hf$ ranging from 0.282829-0.282986, corresponding to $\varepsilon_{Hf}(t)$ from +2.6 to +8.2. Similarly, 15TNM10-2 zircons vary across more than 5 epsilon units, with $\varepsilon_{Hf}(t)$ from +1.6 to +6.6.

4.2 Amphibole mineral chemistry

Major oxide data for amphibole from the Nyemo pluton are given in Table S3. Amphibole from MMEs and their host rocks have similar concentrations of SiO_2, Al_2O_3, FeO, Na_2O and K_2O. However, amphibole in the MMEs have higher average TiO_2 contents and lower average MgO and MnO contents than those in the host rocks. In the B (Na) vs. B (Ca + Na) diagram (Leake, 1978), all analyzed amphibole plots in the calcic field (Fig. 5a). In the diagram of $Mg/(Mg+Fe^{+2})$ vs. Si atoms per formula unit diagram (Leake, 1978), most of the amphibole in Nyemo host rocks plot in or along the edge of the magnesiohornblende field, whereas most of the analyses from the MMEs plot as ferrohornblende (Fig. 5b). In addition, the geochemical diagrams of amphiboles (Fig. 5c-d) imply that some of amphiboles in MMEs are mantle-derived,

except for those amphiboles formed during magma mixing (Jiang and An, 1984), and the relationship of these magmatic systems with subduction (Coltorti et al., 2007).

Amphibole chemistry may be used to infer magmatic temperatures in some circumstances. Based on the thermobarometry of subduction-related amphiboles associated with calc-alkaline magmatism, Ridolfi et al. (2010) proposed a new formulation (T (°C) = −151.487Si*+2041, where $Si^* = Si + {}^{[4]}Al/15 - 2{}^{[4]}Ti - {}^{[6]}Al/2 - {}^{[6]}Ti/1.8 + Fe^{3+}/9 + Fe^{2+}/3.3 + Mg/26 + {}^{B}Ca/5 + {}^{B}Na/1.3 - {}^{A}Na/15 + {}^{A}[]/2.3$). With this formula, amphibole in the Nyemo host rocks yields rather high temperatures, 837-869 °C.

4.3 Whole-rock major and trace elements

Whole rock major and trace element data are given in Table 1. The host rocks of the Nyemo pluton have high SiO_2 (65.9-66.1 wt. %) and K_2O (2.76-4.31%) contents, low MgO (1.25-1.41%) contents and $Mg^{\#}$ (38.5-42.5). Based on total alkalis vs. SiO_2 the compositions plot in the quartz monzonite and granodiorite fields (Fig. 6a). They are metaluminous (Fig. 6b) members of the high-K calc-alkaline series (Fig. 6d). The MME samples have lower SiO_2 (52.9-56.6%), but higher K_2O (3.57-4.53%), $Mg^{\#}$ (43.9-45.5), Cr (26-43 ppm) than their host rocks. MMEs span the fields of monzodiorite and monzonite (Fig. 6a), are metaluminous (Fig. 6b), and belong to the shoshonite series based on K_2O vs SiO_2 (Fig. 6d). For all samples of the Nyemo pluton, the concentrations of MgO, Al_2O_3, CaO and $Fe_2O_3{}^{T}$ decrease with increasing SiO_2, while K_2O correlates positively with SiO_2.

In a chondrite-normalized rare earth element (REE) diagram (Fig. 7a), all the host rocks are enriched in light rare-earth elements (LREEs) and depleted in heavy rare-earth elements (HREEs), with slightly negative Eu anomalies (Eu/Eu* = 0.75-0.81). The MME patterns are nearly parallel to the host rock patterns but are

systematically richer in total REE budget by about a factor of two. A primitive mantle-normalized trace element diagram (Fig. 7b) shows that both the host rocks and MME samples show enrichment of large ion lithophile elements (LILEs) (Rb, Ba, Th, U) and negative anomalies in high field strength elements (HFSEs) (Nb, Ta, P, Ti), with significant positive Pb anomalies. Again, the MMEs are generally richer than the host rocks in concentration of most trace elements.

The low concentrations of HREEs (Yb = 0.62-0.79 ppm) and Y (8.7-10.8 ppm) and the high Sr concentrations (696 -778 ppm) combine to give high Sr/Y ratios (65 - 85) in the high SiO_2 host rocks of the pluton. These characteristics classify the quartz monzonites and granodiorites as adakite-like rocks, as defined by Defant and Drummond (1990) (Fig. 7c).

4.4 Whole-rock Sr-Nd-Pb isotopes

Whole rock Sr-Nd-Pb isotope data are given in Table 1. Initial $^{87}Sr/^{86}Sr$ and $\varepsilon_{Nd}(t)$ values were calculated at 28.5 Ma (average U-Pb weighted age). The host rock samples show relatively homogeneous Sr and Nd isotopic composition with $\varepsilon_{Nd}(t)$ of -2.2 to -2.8 and $^{87}Sr/^{86}Sr_{(i)}$ of 0.7065 to 0.7067 (Fig. 8a) and moderately radiogenic Pb isotopic signatures ($^{206}Pb/^{204}Pb$ = 18.494 - 18.510, $^{207}Pb/^{204}Pb$ = 15.679 - 15.682, and $^{208}Pb/^{204}Pb$ = 38.939 - 38.951) (Figs. 8b-c). The MME samples are identical to their host rocks in $^{87}Sr/^{86}Sr_{(i)}$ (0.7066 to 0.7067) and Pb isotope ratios ($^{206}Pb/^{204}Pb$ = 18.492 - 18.504, $^{207}Pb/^{204}Pb$ = 15.681 - 15.683, and $^{208}Pb/^{204}Pb$ = 38.945 - 38.967) but modestly more radiogenic in Nd, with $\varepsilon_{Nd}(t)$ values of -3.0 to -3.5.

5. Discussion

5.1 Petrogenesis of MMEs

5.1.1 Genetic mechanism

Mafic microgranular enclaves (MMEs) in granitoid plutons, though common, remain enigmatic. There are four main categories of genetic models for MMEs: (1) Dodge and Kistler (1990) proposed that MMEs separated from the same parental magma as their host rocks by early fractional crystallization. Such MMEs would be expected to share analogous mineral compositions, isotopic characteristics, and formation pressure with their hosts. (2) Chen et al. (1989) deemed that some MMEs are residues of the melting process that created their host rocks; such MMEs should have metamorphic textures and similar isotopic compositions to their host rocks (3) Some MMEs are thought to be accidental xenolithic debris (Maas et al., 1997), picked up from country rocks and so with no expectation of isotopic or other similarity to their host rocks. Finally, (4) MMEs may represent mafic liquid derived from the mantle or mafic lower crust that ascended into and incompletely mixed with upper crustal host melts (Zheng et al., 2012). We argue for this last hypothesis, i.e. mixing between mantle-derived and crustally-derived melts, for the MMEs in the Nyemo pluton, for the reasons detailed below.

First, the MMEs in the Nyemo pluton are characterized by elongate or spheroidal shapes and typical fine-granular igneous texture rather than cumulate or metamorphic texture (Fig. 4a). This suggests they were incorporated into the host melt as liquids and argues against other possible origins, such as crystalline restites or xenoliths. The absence of any inherited zircons in the MMEs (or in the host rocks) also argues against a restite or xenolith origin for the MMEs or for the disaggregation of any solid

debris into the pluton. Furthermore, the abundant needle-like apatite and the growth of K-feldspar megacrysts across the boundaries between MMEs and host rocks indicate that MMEs were intruded as hot mafic magmas that quenched against cooler felsic magma (Reid et al., 1983). In many (but not all) compositional components, the MMEs and host rocks plot along single roughly linear trends with a large gap between the most evolved MME and the most primitive host rock (Fig. 6). This pattern is consistent with partial chemical mixing between the two liquids. The mixing lines are imperfect for easy mobilized elements such as alkalis, which might have been modified and displaced from linear mixing trends by post-magmatic hydrothermal activity or weathering.

On a plot mixing diagnostic plots such as FeO^T vs. MgO (Fig. 9a) and $1/C_c$ versus C_i/C_c diagrams(Fig. 9b) (where "i" represents an incompatible element, and "c" represents a compatible element), the MMEs and host rocks lie close to simple binary mixing trends consistent with a hybrid origin (Schiano et al., 2010; Zorpi et al., 1989). Moreover, MMEs and high Sr/Y host rocks show nearly parallel chondrite- and primitive mantle-normalized patterns, which may reflect the efficiency of elemental diffusion and homogenization in the liquid and partially molten states (Fig. 7). On the amphibole Al_2O_3 vs. TiO_2 diagram, which has been applied to discriminating the origin of parental magma, most amphibole analyses in the Nyemo samples point to a crust-mantle mixed source (Jiang and An, 1984), but some of amphibole analyses in MMEs point to a mantle source (Fig. 5d).

Turning to isotopic tests of the relationship between the MMEs and the host magma, we note that zircons are highly resistant to re-equilibration during magma mixing. Hence, we might expect Hf isotope ratios measured in zircon to retain original source signatures to a significant extent, even if diffusion has largely

homogenized whole-rock isotope ratios throughout the pluton and between MME and host magma (Griffin et al., 2002). Hence, the heterogeneous Hf composition (ranges of 6 to 7 epsilon units) of zircons in both MMEs and host rocks indicate a hybrid magma source (Fig. 4). In a similar vein, the observation of identical $(^{87}Sr/^{86}Sr)_i$ ratios but distinct ε_{Nd} between the MMEs and host high Sr/Y rocks (Fig. 8a) is consistent with the expectation that Sr isotopes equilibrate more rapidly than Nd isotopes during magma mixing (Elburg, 1996). Consequently, the hypothesis that MMEs in the Nyemo pluton are the product of (and demonstrate the action of) magma mixing is preferred.

5.1.2 Evaluation of crustal contamination

To use the geochemical data effectively for probing the magma source of MMEs, we need to evaluate whether assimilation of crustal components, including the host pluton magma itself, have erased or strongly modified evidence of their mantle source compositions. In this context the fact the MMEs have higher concentrations of Rb (163 - 185 ppm) and Ba (714 - 1127 ppm) than those of average continental crust (49 ppm Rb and 456 ppm Ba) argues against bulk assimilation of continental crust (Zhao et al.,2009), though it does not exclude assimilation of a small-degree melt of the crust. However, assimilation of either bulk crust or crustal melt will inevitably lead to an increase in $(^{87}Sr/^{86}Sr)_i$ and a decrease in $\varepsilon_{Nd}(t)$, whereas the distribution of these isotopes in the MMEs are quite limited and Nd is in fact more rather than less radiogenic in the MMEs compared to the host rocks. There is no significant linear correlation between $\varepsilon_{Nd}(t)$ and SiO_2 within the MMEs (Fig. 6e). In addition, the Hf isotope ratios of zircons in the MMEs show depleted characteristics (Fig. 8d), inconsistent with major modification of the Hf content of the MME parent magma by

crustal contamination. Turning to the host pluton magma itself, there would display a successive variation in the Harker diagrams if there is a high-degree assimilation to mafic enclaves from their host rocks, which is inconsistent with the large gap between the most evolved MME and the most primitive host rock. Besides, mafic enclaves generally show a greater abundance of LILEs (e.g., Rb, Ba, Th, U, Pb, and Sr) and LREEs than their host rocks, indicating that these abundances are a primary feature of the enclaves rather than an influence of the host rock.

5.1.3 Origin of enriched signature

The MMEs in Nyemo pluton have relatively low SiO_2 alongside high Al_2O_3 (17.3-18.5%), K_2O (3.57-4.53%), K_2O+Na_2O (8.22-8.91%), and K_2O/Na_2O (0.74-1.06). Their alkali contents and ratios place them firmly in the shoshonite series (Figs 6d and 10a). Moreover, their highly enriched LILE concentrations and trace elements discrimination diagrams confirm the shoshonitic affinity of the MMEs (Fig. 10b) (Müller et al., 1992).

The magmatic origin of shoshonitic rocks is controversial. Some have argued that shoshonitic magma originate from dehydration melting of enriched metabasaltic amphibolite at the base of the crust (Pe-Piper et al., 2009). Most authors, though, have proposed that shoshonitic rocks are derived from low-degree melts of hydrous and enriched mantle (Zhao et al., 2009), consistent with the experimental results of Wyllie and Sekine (1982). Peccerillo (1992) specifically suggested that the sources of shoshonitic rocks are lithospheric mantle domains previously metasomatized by subduction-related fluids or melts. Some theories that picture a mantle origin have emphasized that later fractionation and crustal assimilation are in fact the dominant processes by which these rocks acquire their shoshonitic character (Feeley and Cosca,

2003). Since the MMEs show more enriched Nd and Hf isotope ratios and significantly higher incompatible trace element contents than their felsic host rocks, it appears in this case that the mantle-derived mafic end-member magma was more enriched than the (likely crustal) felsic end-member magma that it mixed with. Enriched components that might have affected the mantle beneath the Lhasa terrane include: (1) recycled mantle components unrelated to the local tectonic environment, (2) the ancient continental basement of the Lhasa terrane (Liu et al., 2017), (3) melt or fluid derived from subducted Neo-Tethys oceanic sediments (Guo et al., 2007), and (4) Indian continental crust (Ding et al., 2003; Zhao et al., 2009). For the reasons developed below, we propose that Indian continental materials formed the main enrichment agents for the source of the Oligocene MMEs in the Nyemo pluton.

Although unrelated mantle components might always be arbitrarily invoked to explain enrichment, this idea is essentially untestable, provides no insight into the local geological history, and is unnecessary in the rich tectonic environment of Tibet, so we do not consider this idea further. Ancient continental basement of the Lhasa terrane is rarely exposed in southern Lhasa terrane and may not be present at depth so far south, presently or in the Oligocene. Most magmas emplaced in the area from the Cretaceous to the Oligocene show depleted zircon Hf isotopes, which argues against ancient basement at depth (Ji et al., 2009). Given the low Hf contents of oceanic sediment, mixing calculations require that the source would need to consist of an excessively high proportion of sediment (50-60%) to yield the ε_{Hf} of the MMEs if oceanic sediment were the sole enrichment agent. This is unreasonable from a major element perspective, given the low SiO_2 contents of MMEs (Ma et al., 2017), which suggests that subducted oceanic sediment is not the principal source of enrichment. Considering the list of possible enrichment agents, we are left with subducted or

underthrust Indian continental crust material as the most likely suitable source.

Although ε_{Hf} and ε_{Nd} are generally correlated because in each isotopic system the parent element is more compatible than the daughter, the MMEs have positive ε_{Hf} but negative ε_{Nd}. This signature can be attributed to the retention of unradiogenic Hf in residual zircon during melting of the Indian continental crust, creating a metasomatic agent that will be much more effective at modifying Nd signatures (Chu et al., 2011). The contribution of the Indian continental crust to the enrichment of the MMEs source region can be further indicated by the relationship between the whole rock Nd isotope and trace element signatures (Fig. 10c). Himalayan leucogranites are more depleted in Y, HREEs and more enriched in incompatible elements than high Sr/Y rocks in southern Tibet, suggesting that the high Rb/Sr in the low $^{143}Nd/^{144}Nd$ high Sr/Y samples can be explained by incorporation of Indian crust components (Liu et al., 2017). The role of melting, as opposed to dehydration, in mobilizing the enrichment signature from the Indian continental material is emphasized by the preferential enrichment of melt-mobile (e.g. Nb) over fluid-mobile (e.g. Rb) elements in the MMEs (Castillo and Newhall, 2004) (Fig. 10d).

Our proposed source enrichment model for the Nyemo MMEs is in agreement with other research on post-collisional mafic magmas in the southern Lhasa terrane. The 35 Ma Quguosha gabbro has similar isotopic and geochemical characteristics and has also attributed to melting of Tibetan lithospheric mantle metasomatized by melt of subducted Indian sediment (Ma et al., 2017). The survey of $\varepsilon_{Hf}(t)$ of co-magmatic zircons separated from post-collisional magmatic rocks in southern Tibet by Liu et al (2017) found a sharp drop at 35 Ma, interpreted to mark the arrival of material derived from Indian continental crust in post-collisional magmatic systems in Tibet.

5.1.4 Mineralogy of metasomatized lithospheric mantle

It is noteworthy that the MMEs differ from melts derived from mantle peridotite in having low contents of MgO (2.64 - 3.36 %), Cr (25.6-43.2 ppm) and Ni (18.5 - 29.7 ppm) (Rapp et al., 1999) (Fig. 6c). The simplest explanation for this observation is a source composed of pyroxenites rather than peridotites in the metasomatized lithospheric mantle (Clemens et al., 2017). Furthermore, the MMEs are characterized by strong depletion in HREEs, conventionally taken to indicate the presence of garnet or amphibole in the source region (or during fractionation) (Fig. 7a). Because amphiboles often preferentially incorporate MREEs compared to HREEs (Davidson et al., 2007), U-shaped chondrite-normalized patterns are specifically associated with residual or fractionated amphiboles. The Nyemo MMEs do not show U-shaped patterns, pointing to garnet as a complementary HREE reservoir to these melts. Furthermore, the MMEs exhibit high Rb/Sr (> 0.19) and low Ba/Rb (< 7) ratios, which indicate that the main potassic phase in the source region is phlogopite rather than potassic amphibole. Melts derived from phlogopite-bearing mantle are expected to have significantly higher Rb/Sr (> 0.1) and lower Ba/Rb (< 20) ratios than those derived from amphibole-bearing mantle sources (Rb/Sr < 0.06, Ba/Rb > 20) (Davidson et al., 2007) (Fig. 10e). Consequently, major and trace element chemistry together suggest a source region for the MMEs mainly composed of phlogopite, garnet and pyroxene. This motivates a test using batch melting of a garnet-phlogopite clinopyroxenite xenolith (40% clinopyroxene, 55% garnet and 5% phlogopite, with 21 ppm Rb and 562 ppm Cr; from Liu et al., (2003) as a source model. Several of the MME whole-rock compositions plot in the sensitive Rb (a highly incompatible elements) vs. Cr (a highly compatible element) diagram along this model trend at 5%-7% batch partial melting (Fig. 10f).

5.2 Generation of adakitic signatures in the high Sr/Y host rocks

The main quartz monzonite-granodiorite phase of the Nyemo pluton has adakitic affinity, indicated by high SiO_2 and Sr, but low Y and Yb. The origin of adakitic signatures (e.g., high Sr/Y and La/Yb ratios) in Oligocene Tibetan granitoids is still obscure. It is widely known that adakitic affinity can be generated by a variety of mechanisms, including crustal assimilation and low-pressure fractional crystallization (involving amphibole) from parental basaltic magmas (Xu et al., 2015); high-pressure crystallization (involving garnet) of mafic magmas (Macpherson et al., 2006); magma mixing between felsic and basaltic magmas (Streck et al., 2007); partial melting of (i) thickened lower crust (Hou et al., 2004), (ii) Indian continental crust (Xu et al., 2010), (iii) subducted Neo-Tethyan oceanic crust (Qu et al., 2004), (iiii) delaminated lower crust (Wang et al., 2004). For the reasons outlined below, we conclude that melting of the thickened Gangdese crust and fractional crystallization of zircon offers the best explanation for the character of the Nyemo pluton.

First, the positive correlation between $\varepsilon_{Nd}(t)$ and SiO_2 of high Sr/Y host rocks exclude the possibility of significant crustal contamination from upper crust. As for fractional crystallization, major modification of hydrous melts by low-pressure amphibole fractionation is unlikely because the MREE and HREE contents of the host rocks do not show U-shaped patterns consistent with amphibole fractionation (Davidson et al., 2007). The Dy/Yb ratios should increase with increasing SiO_2 with significant fractionation of garnet. However, there is no obvious correlation between them, which is not in accord with garnet fractionation. Additionally, the La/Sm and La/Yb ratios of the host rocks both increase with the increase of La further exclude the fractional crystallization as the major modification. Finally, only small volumes of coeval mafic magma have been identified in the Lhasa terrane (Ding et al., 2018),

which are inadequate to support derivation of large volumes of evolved high Sr/Y plutons by fractional crystallization. It is noteworthy that Sr/Y increases with increasing SiO_2 in high Sr/Y host rocks (Fig. 6f), which suggests the fractional crystallization may play a role in the high Sr/Y feature. As discussed above, the host rocks did not experience significant crystallization of hornblende and garnet. We consider it as the result of zircon fractionation (Sr and Y partition coefficient for zircon is 0.034 and 50.2 respectively.) (Thomas et al., 2002), which is supported by the negative correlation between SiO_2 and Zr concentrations.

The similarity in trace element patterns between the MMEs and the host rock and the severe depletion of HREEs and Y in the MMEs suggests that mixing of a mafic end member into the main magma of the pluton might lead to adakitic signatures. However, Sr/Y actually increases with increasing SiO_2 (Fig. 6f), pointing away from the MMEs as adakitic signatures becomes more defined. Therefore, we proposed that Nyemo host rocks may be generated by partial melting. The host quartz monzonites show low concentrations of MgO, Cr, and Ni and low $Mg^{\#}$ (<42.5). Experiments have shown that melts basaltic sources at high pressure (>1 GPa) may begin with Mg# $\leqslant$ 44 but that interaction with peridotite will increase their $Mg^{\#}$ to ~55 (Rapp et al., 1999). The low concentrations of MgO and compatible elements show that, unless strongly modified by later fractionation, the magma did not interact with mantle peridotite on ascent. This argues against their derivation from either subducted Neo-Tethyan oceanic crust, Indian continental crust because these components would melt below the mantle wedge and the derived melts would have to ascend peridotite (Rapp et al., 1999). Besides, melts from delaminated lower crust will inevitably interact with the mantle peridotite while they ascend, resulting in significantly high concentrations of Cr, Ni and MgO, which is not observed in the high Sr/Y host rocks.

These considerations point towards thickened lower crust with residual garnet as the source for the high Sr/Y magma as illustrated in Fig.7c.

The major element discrimination scheme proposed by Altherr and Siebel (2002) and Patiño Douce (1999) (Fig. 11a) places the high Sr/Y Nyemo host rocks in the field of metabasalt-derived melts, alongside many other samples in our compilation that have been assigned to dehydration melting of lower crust. Trace elements ratios of Ba, La, and Nb in the high Sr/Y host rocks overlap with the field of continental arc volcanic rocks more than with average continental crust, consistent with their origin in crust developed by extended subduction before delamination of the mafic lower crust (Fig. 11b).

5.3 Constraints on the timing of the onset of extension of the southern Lhasa terrane

Numerous studies have attributed the generation of the post-collisional magmas, The main geodynamic models have been proposed to explain orogenic uplift and post-collisional magmatism in Tibet, emphasize either convective removal of sub-continental lithospheric mantle (Zhao et al., 2009) or break-off or roll-back of the subducted Indian plate (Zhang et al., 2014). No such north-south trend has been found in intrusive or eruption ages, which argues against the slab roll-back idea. Besides, the breakoff of the Indian continental slab calls for extensive potassic and high Sr/Y magmatism with adakitic affinity , which emplaced intensively in 25 to 8 Ma (Zhao et al., 2009), later than Nyemo pluton. Therefore, we suggest that convective removal of sub-continental lithospheric mantle is most likely responsible for voluminous post-collisional magmatism in the Lhasa terrane in general and for the Nyemo pluton in particular.

Previous studies have shown that post-collisional potassic and high Sr/Y with

adakitic affinity rocks, with same similar age range and a close correlation to a series of N–S-trending rifts within Lhasa terrane, are related to the east–west extension of (Guo et al.,2007; Hou et al., 2004). The onset of east - west extension is commonly manifested as convective removal the thickened Tibetan lithosphere (Zhao et al., 2009), when the Tibetan Plateau achieved its highest elevation and the tectonics collapse subsequently. Therefore, the post-collisional potassic and high Sr/Y with adakitic affinity magmatism may provide constraint on the timing of the uplift and onset of extension of the Tibetan Plateau (Guo et al.,2007)

It is generally accepted that post-collisional, K-rich magmatism only occurred between 25 and 8 Ma, which may signal the onset of extension in south Tibet at ~25 Ma (Guo et al., 2013). In this paper, we have identified shoshonitic rocks exposed as mafic enclaves, entrained by high Sr/Y pluton with adakitic affinity in southern Lhasa terrane at ~30Ma, signifying that the transition from compression (related to India–Eurasia collision since ~65–50 Ma) to tectonic extension of southern Lhasa terrane begins around 30Ma rather than 25Ma. Additionally, existence of shoshonitic mafic enclaves in the Oligocene(~30Ma) Chongmuda-Mingze intrusive complex of southern Lhasa terrane (Zheng et al., 2012) further supports this idea.

(Chung et al.,2009) proposed that La/Yb ratios can be used for estimating the crustal thickness. In this paper, we plotted La/Yb ratios versus ages of post-collisional high Sr/Y rocks with adakitic affinity in southern Lhasa terrane. The figure 12 display that the La/Yb ratios of post-collisional high Sr/Y rocks with adakitic affinity reached the peak at ~30Ma, suggesting that the southern Lhasa terrane probably have the thickest crust during late Oligocene. Combined the fact that the onset of the potassic magmatism at ~30Ma, we proposed that the tectonic extension of southern Lhasa terrane begins around 30Ma the late Oligocene.

6. Conclusion

(1) Zircon U–Pb ages indicate that the main high Sr/Y phase of the Nyemo pluton and its shoshonitic mafic microgranular enclaves formed almost simultaneously at ~28 Ma.

(2) The high Sr/Y host rocks are derived from partial melting of the thickened lower crust of Lhasa terrane, whereas the shoshonitic mafic microgranular enclaves were produced by low-degree melting of an enriched lithospheric mantle beneath the Lhasa terrane.

(3) The occurrence of shoshonitic magma and high La/Yb and high Sr/Yhost rocks with adakitic affinity indicate the onset of extension and convective removal of Tibetan lithosphere around 30 Ma.

Acknowledgements

We thank editor Xian-Hua Li for handling this manuscript and two anonymous reviewers for constructive comments. We are grateful to Liyuan Xing and Yan Tang for assistance of fieldwork in Tibet and geochemical analyses. This research was supported by the Second Tibetan Plateau Scientific Expedition and Research (STEP) program (grant 2019QZKK0702), the National Key Research and Development Project of China (project 2016YFC0600304), the Natural Science Foundation of China (grant 41802058), the Fundamental Research Funds for the Central Universities (grants 2652018122 and QZ05201902), and the 111 Project of the Ministry of Science and Technology of China (projects BP0719021 and B18048). ZW acknowledges a fellowship from the China Scholarship Council (CSC No. 201806400019).

References:

Altherr, R., Siebel, W., 2002. I-type plutonism in a continental back-arc setting: Miocene granitoids and monzonites from the central Aegean Sea, Greece. Contributions to Mineralogy and Petrology 143, 397-415.

Armstrong, J.T., 1995. CITZAF — a package of correction programs for the quantitative Electron Microbeam X-Ray-Analysis of thick polished materials, thin-films, and particles. Microbeam Analysis 4, 177-200.

Boynton, W.V., 1984. Cosmochemistry of the rare earth elements: meteorite studies, Developments in geochemistry. Elsevier, pp 63-114.

Castillo, P.R., Newhall, C.G., 2004. Geochemical constraints on possible subduction components in lavas of Mayon and Taal volcanoes, southern Luzon, Philippines. Journal of Petrology 45, 1089-1108.

Chen, Y.D., Price, R.C., White, A., 1989. Inclusions in three S-type granites from southeastern Australia. Journal of Petrology 30, 1181-1218.

Chu, M., Chung, S., O'Reilly, S.Y., Pearson, N.J., Wu, F., Li, X., Liu, D., Ji, J., Chu, C., Lee, H., 2011. India's hidden inputs to Tibetan orogeny revealed by Hf isotopes of Transhimalayan zircons and host rocks. Earth and Planetary Science Letters 307, 479-486.

Chung, S.L., Chu, M.F., Ji, J., O'Reilly, S.Y., Pearson, N.J., Liu, D., Lo, C.H., 2009. The nature and timing of crustal thickening in Southern Tibet: Geochemical and zircon Hf isotopic constraints from postcollisional adakites. Tectonophysics 477, 36-48.

Clemens, J.D., Buick, I.S., Frei, D., Lana, C., Villaros, A., 2017. Post-orogenic shoshonitic magmas of the Yzerfontein pluton, South Africa: the 'smoking gun' of mantle melting and crustal growth during Cape granite genesis?

Contributions to Mineralogy and Petrology 172, 72.

Coltorti, M., Bonadiman, C., Faccini, B., Grégoire, M., O'Reilly, S. Y., Powell, W., 2007. Amphiboles from suprasubduction and intraplate lithospheric mantle. Lithos 99, 68-84.

Dai, J., Wang, C., Polat, A., Santosh, M., Li, Y., Ge, Y., 2013. Rapid forearc spreading between 130 and 120 Ma: evidence from geochronology and geochemistry of the Xigaze ophiolite, southern Tibet. Lithos 172, 1-16.

Davidson, J., Turner, S., Handley, H., Macpherson, C., Dosseto, A., 2007. Amphibole "sponge in arc crust? Geology 35, 787-790.

Defant, M.J., Drummond, M.S., 1990. Derivation of some modern arc magmas by melting of young subducted lithosphere. Nature 347, 662.

Ding, H.X., Zhang, Z.M., 2018. Early Cenozoic thickening and reworking of the eastern Gangdese arc, south Tibet: constraints from the Oligocene granitoids. Geological Society, London, Special Publications 474, SP474. 5.

Ding, L., Kapp, P., Zhong, D., Deng, W., 2003. Cenozoic volcanism in Tibet: evidence for a transition from oceanic to continental subduction. Journal of Petrology 44, 1833-1865.

Dodge, F., Kistler, R.W., 1990. Some additional observations on inclusions in the granitic rocks of the Sierra Nevada. Journal of Geophysical Research: Solid Earth 95, 17841-17848.Elburg, M.A., 1996. Evidence of isotopic equilibration between microgranitoid enclaves and host granodiorite, Warburton Granodiorite, Lachlan Fold Belt, Australia. Lithos 38, 1-22.

Feeley, T.C., Cosca, M.A., 2003. Time vs. composition trends of magmatism at Sunlight volcano, Absaroka volcanic province, Wyoming. Geological Society of America Bulletin 115, 714-728.

Furman, T., Graham, D., 1999. Erosion of lithospheric mantle beneath the East African Rift system: geochemical evidence from the Kivu volcanic province Developments in Geotectonics. Elsevier 24, 237-262.

Gao, Y., Hou, Z., Kamber, B.S., Wei, R., Meng, X., Zhao, R., 2007. Lamproitic rocks from a continental collision zone: evidence for recycling of subducted Tethyan oceanic sediments in the mantle beneath southern Tibet. Journal of Petrology, 48, 729–752.

Griffin, W.L., Wang, X., Jackson, S.E., Pearson, N.J., O'Reilly, S.Y., Xu, X., Zhou, X., 2002. Zircon chemistry and magma mixing, SE China: in-situ analysis of Hf isotopes, Tonglu and Pingtan igneous complexes. Lithos 61, 237-269.

Guo, F., Nakamura, E., Fan, W., Kobayashi K., Li, C., 2007. Generation of Palaeocene adakitic andesites by magma mixing; Yanji Area, NE China. Journal of Petrology 48, 661-692.

Guo, Z., Wilson, M., Zhang, M., Cheng, Z.Zhang, L., 2013. Post-collisional, K-rich mafic magmatism in south Tibet: constraints on Indian slab-to-wedge transport processes and plateau uplift. Contributions to Mineralogy and Petrology 165, 1311 -1340Hou, Z.Q., Gao, Y.F., Qu, X.M., Rui, Z.Y., Mo, X.X., 2004. Origin of adakitic intrusives generated during mid-Miocene east–west extension in southern Tibet. Earth and Planetary Science Letters 220, 139-155.

Houseman, G.A., McKenzie, D.P., Molnar, P., 1981. Convective instability of a thickened boundary layer and its relevance for the thermal evolution of continental convergent belts. Journal of Geophysical Research: Solid Earth 86, 6115-6132.

Ji, W., Wu, F., Chung, S., Li, J., Liu, C., 2009. Zircon U–Pb geochronology and Hf isotopic constraints on petrogenesis of the Gangdese batholith, southern Tibet.

Chemical Geology 262, 229-245.

Jiang, C.Y., An, S.Y., 1984. On chemical characteristics of cal-cic amphiboles from igneous rocks and their petrogenesis significance. Journal of Mineralogy and Petrology 3, 1-9.

Jiang, Y.H., Jiang, S.Y., Ling, H.F., Dai, B.Z., 2006. Low-degree melting of a metasomatized lithospheric mantle for the origin of Cenozoic Yulong monzogranite-porphyry, east Tibet: geochemical and Sr–Nd–Pb–Hf isotopic constraints. Earth and Planetary Science Letters 241, 617-633.

Leake, B.E., 1978. Nomenclature of amphiboles. *American Mineralogist*, *63*(11-12), 1023-1052.

Liu, D., Zhao, Z., DePaolo, D.J., Zhu, D.C., Meng, F.Y., Shi, Q., Wang, Q., 2017. Potassic volcanic rocks and adakitic intrusions in southern Tibet: Insights into mantle–crust interaction and mass transfer from Indian plate. Lithos 268, 48-64.

Liu, X. F., Liu, J.D., Zhang, C.J., Wu, D.D., Li, Y.G., Liu, J.D., Yang, Z.X., 2003. Study on elemental geochemistry of ultramafic deep xenoliths in alkali-rich porphyry. Mineral Petrology 23, 39-43. (in Chinese with English abstract).

Liu, Y.S., Zong, K.Q., Kelemen, P.B., Gao, S., 2008. Geochemistry and magmatic history of eclogites and ultramafic rocks from the Chinese continental scientific drill hole: subduction and ultrahigh-pressure metamorphism of lower crustal cumulates. Chemical Geology 247, 133–153.

Liu, Y., Hu, Z., Zong, K., Gao, C., Gao, S., Xu, J., Chen, H., 2010. Reappraisement and refinement of zircon U-Pb isotope and trace element analyses by LA-ICP-MS. Chinese Science Bulletin 55, 1535-1546.

Ma, L., Wang, Q., Li, Z.X., Wyman, D.A., Yang, J.H., Jiang, Z.Q., Guo, H.F., 2017.

Subduction of Indian continent beneath southern Tibet in the latest Eocene (~ 35 Ma): Insights from the Quguosha gabbros in southern Lhasa block. Gondwana Research 41, 77-92.

Ma, L., Wang, Q., Wyman, D.A., Jiang, Z., Yang, J., Li, Q., Gou, G., Guo, H., 2013. Late Cretaceous crustal growth in the Gangdese area, southern Tibet: Petrological and Sr–Nd–Hf–O isotopic evidence from Zhengga diorite–gabbro. Chemical Geology 349-350, 54-70.

Maas, R., Nicholls, I.A., Legg, C., 1997. Igneous and metamorphic enclaves in the S-type Deddick Granodiorite, Lachlan Fold Belt, SE Australia: petrographic, geochemical and Nd-Sr isotopic evidence for crustal melting and magma mixing. Journal of Petrology 38, 815-841

Macpherson, C.G., Dreher, S.T., Thirlwall, M.F., 2006. Adakites without slab melting: high pressure differentiation of island arc magma, Mindanao, the Philippines. Earth and Planetary Science Letters 243, 581-593.

Maniar, P.D., Piccoli, P.M., 1989. Tectonic discrimination of granitoids. Geological Society of America Bulletin 101, 635-643.

Martin, H., Smithies, R.H., Rapp, R., Moyen, J.F., Champion, D., 2005. An overview of adakite, tonalite–trondhjemite–granodiorite (TTG), and sanukitoid: relationships and some implications for crustal evolution. Lithos 79, 1-24.

Middlemost, E.A.K., 1994. Naming materials in the magma/igneous rock system. Annual Review of Earth and Planetary Sciences 37, 215-224.

Muir, R.J., 1995. Geochemistry of the Cretaceous Separation Point Batholith, New Zealand: granitoid magmas formed by melting of mafic lithosphere. Journal of the Geological Society 152, 689-701.

Müller, D., Rock, N., Groves, D.I., 1992. Geochemical discrimination between

shoshonitic and potassic volcanic rocks in different tectonic settings: a pilot study. Mineralogy and Petrology 46, 259-289.

Pan, G.T., 2006. Spatial temporal framework of the Gangdese Orogenic Belt and its evolution. Acta Petrologica Sinica 22, 521-533. (in Chinese with English abstract).

Patiño Douce, A.E., 1999. What do experiments tell us about the relative contributions of crust and mantle to the origin of granitic magmas? Geological Society, London, Special Publications 168, 55-75.

Pearce, J.A., 1983. Role of the sub-continental lithosphere in magma genesis at active continental margins, 230-249.

Peccerillo, A., 1992. Potassic and ultrapotassic rocks-compositional characteristics, petrogenesis, and geological significance. Episodes 15, 243-251.

Peccerillo, A., Taylor, S.R., 1976. Geochemistry of Eocene calc-alkaline volcanic rocks from the Kastamonu area, Northern Turkey. Contributions to Mineralogy and Petrology 58 (1), 63–81.

Petford, N., Atherton, M., 1996. Na-rich Partial Melts from Newly Underplated Basaltic Crust: The Cordillera Blanca Batholith, Peru. Journal of Petrology 37, 1491-1521.

Pe-Piper, G., Piper, D.J., Koukouvelas, I., Dolansky, L.M., Kokkalas, S., 2009. Postorogenic shoshonitic rocks and their origin by melting underplated basalts: The Miocene of Limnos, Greece. Geological Society of America Bulletin 121, 39-54.

Qu, X., Hou, Z., Li, Y., 2004. Melt components derived from a subducted slab in late orogenic ore-bearing porphyries in the Gangdese copper belt, southern Tibetan plateau. Lithos 74, 131-148.

Rapp, R.P., Shimizu, N., Norman, M.D., Applegate, G.S., 1999. Reaction between slab-derived melts and peridotite in the mantle wedge: experimental constraints at 3.8 GPa. Chemical Geology 160, 335-356.

Richards, J. P., Kerrich, R., 2007. Special paper: adakite-like rocks: their diverse origins and questionable role in metallogenesis. Economic Geology 102, 537-576.

Ridolfi, F., Renzulli, A., Puerini, M., 2010. Stability and chemical equilibrium of amphibole in calc-alkaline magmas: an overview, new thermobarometric formulations and application to subduction-related volcanoes. Contributions to Mineralogy and Petrology 160, 45-66.

Schiano, P., Monzier, M., Eissen, J.P., Martin, H. Koga, K.T., 2010. Simple mixing as the major control of the evolution of volcanic suites in the Ecuadorian Andes. Contributions to Mineralogy and Petrology 160, 297-312.

Stern, C.R., Kilian, R., 1996. Role of the subducted slab, mantle wedge and continental crust in the generation of adakites from the Andean Austral Volcanic Zone. Contributions to mineralogy and petrology 123, 263-281.

Streck, M.J., Leeman, W.P., Chesley, J., 2007. High-Mg andesite from Mount Shasta: a product of magma mixing and contamination, not a primitive mantle melt. Geology 35, 351.

Sun, S.S., McDonough, W.F., 1989. Chemical and isotopic systematics of oceanic basalts: implications for mantle composition and processes. Geological Society, London, Special Publications 42.1, 313-345.

Tanaka, T., Togashi, S., Kamioka, H., Amakawa, H., Kagami, H., Hamamoto, T., Yuhara, M., Orihashi, Y., Yoneda, S., Shimizu, H., Kunimaru, T., Takahashi, K., Yanagi, T., Nakano, T., Fujimaki, H., Shinjo, R., Asahara, Y., Tanimizu, M.,

Dragusanu, C., 2000, JNdi-1: a neodymium isotopic reference in consistency with LaJolla neodymium, Chemical Geology 168, 279-281.

Taylor, S. R., McLennan, S. M., 1985. The continental crust: its composition and evolution Blackwell Scientific Publications 54, 209-230 and 372.

Thomas, J. B., Bodnar, R. J., Shimizu, N., Sinha, A. K., 2002. Determination of zircon/melt trace element partition coefficients from SIMS analysis of melt inclusions in zircon. Geochimica et Cosmochimica Acta 66, 2887-2901.

Todt, W., Cliff, R. A., Hanser, A., Hofmann, A. W., 1996, Evaluation of a $^{202}Pb - ^{205}Pb$ Double Spike for High-Precision Lead Isotope Analysis, in A. Basu & S. Hart (eds.), Earth Processes: Reading the Isotopic Code, Geophysical Monograph 95, American Geophysical Union.

Wang, Q., Li, X., Jia, X., Wyman, D., Tang, G., Li, Z., Ma, L., Yang, Y., Jiang, Z., Gou, G., 2012. Late Early Cretaceous adakitic granitoids and associated magnesian and potassium- rich mafic enclaves and dikes in the Tunchang–Fengmu area, Hainan Province (South China): Partial melting of lower crust and mantle, and magma hybridization. Chemical Geology 328, 222-243.

Wang, Q., Zhao, Z., Xu, J., Bai, Z., Wang, J., Liu, C., 2004. The geochemical comparison between the Tongshankou and Yinzu adakitic intrusive rocks in southeastern Hubei(delaminated) lower crustal melting and the genesis of porphyry copper deposit. Acta Petrologica Sinica 20, 351-360.

Wei, Y., Zhao, Z., Niu, Y., Zhu, D., Liu, D., Wang, Q., Hou, Z., Mo, X., Wei, J., 2017. Geochronology and geochemistry of the Early Jurassic Yeba Formation volcanic rocks in southern Tibet: Initiation of back-arc rifting and crustal accretion in the southern Lhasa Terrane. Lithos 278, 477-490.

Wiedenbeck, M., Alle, P., Corfu, F., Griffin, W.L., Meier, M., Oberli, F.V., Quadt, A.V.,

Roddick, J.C.Spiegel, W., 1995. Three natural zircon standards for U- Th- Pb, Lu- Hf, trace element and REE analyses. Geostandards newsletter 19, 1-23.

Wilson, M., 2001. Igneous Petrogenesis. Unwin Hyman, London.

Woodhead, J.D., Hergt, J.M., Simonson, B.M., 1998. Isotopic dating of an Archean bolide impact horizon, Hamersley Basin, Western Australia. Geology 26, 47-50.

Xu, W., Zhang, H., Luo, B., Guo, L., Yang, H., 2015. Adakite-like geochemical signature produced by amphibole-dominated fractionation of arc magmas: An example from the Late Cretaceous magmatism in Gangdese belt, south Tibet. Lithos 232, 197-210.

Xu, W., Zhang, H., Guo, L., Yuan, H., 2010. Miocene high Sr/Y magmatism, south Tibet: Product of partial melting of subducted Indian continental crust and its tectonic implication. Lithos 114, 293-306.Yin, A., Harrison, T.M., 2000. Geologic evolution of the Himalayan-Tibetan orogen. Annual Review of Earth and Planetary Sciences 28, 211-280.

Zhang, L.Y., Ducea, M.N., Ding, L., Pullen, A., Kapp, P., Hoffman, D., 2014. Southern Tibetan Oligocene–Miocene adakites: A record of Indian slab tearing. Lithos 210, 209-223.

Zhao, Z., Mo, X., Dilek, Y., Niu, Y., DePaolo, D.J., Robinson, P., Zhu, D., Sun, C., Dong, G., Zhou, S., 2009. Geochemical and Sr–Nd–Pb–O isotopic compositions of the post-collisional ultrapotassic magmatism in SW Tibet: petrogenesis and implications for India intra-continental subduction beneath southern Tibet. Lithos 113, 190–212.

Zheng, Y., Hou, Z., Li, W., Liang, W., Huang, K., Li, Q., Sun, Q., Fu, Q., Zhang, S., 2012. Petrogenesis and Geological Implications of the Oligocene

Chongmuda-Mingze Adakite-Like Intrusions and Their Mafic Enclaves, Southern Tibet. The Journal of Geology 120, 647-669.

Zhu, D., Pan, G., Chung, S., Liao, Z., Wang, L., Li, G., 2008. SHRIMP zircon age and geochemical constraints on the origin of Lower Jurassic volcanic rocks from the Yeba Formation, southern Gangdese, South Tibet. International Geology Review 50, 442-471.

Zhu, D., Zhao, Z., Niu, Y., Mo, X., Chung, S., Hou, Z., Wang, L., Wu, F., 2011. The Lhasa Terrane: Record of a microcontinent and its histories of drift and growth. Earth and Planetary Science Letters 301, 241-255.

Zorpi, M.J., Coulon, C., Orsini, J.B., Cocirta, C., 1989. Magma mingling, zoning and emplacement in calc-alkaline granitoid plutons. Tectonophysics 157, 315-329.

Figure Captions

Figure 1. Maps of the research area. (a, bottom left) Tectonic subdivision of Tibetan Plateau (Zhu et al., 2011; Pan et al., 2006). The topographic base is from https://www.iedadata.org/; box indicates are shown in next panel. (b, top) Simplified distribution map of post-collisional high Sr/Y rocks with adakitic affinity and ultrapotassic rocks in the Lhasa terrane (Zheng et al., 2012); small box indicates area shown in next panel. (c) Simplified geological map of the Nyemo area in southern Tibet; sample locations are indicated by yellow stars. The names and abbreviations of major suture zones and regional faults are given in the text. NL: northern Lhasa terrane; CL: central Lhasa terrane; SL: southern Lhasa terrane.

Figure 2. Field and petrographic photos. (a) Field photograph of microgranular mafic inclusions (MMEs) showing elliptical forms; red outlines indicate K-feldspar phenocrysts that cross the boundaries of the MMEs. (b) Hand specimen photograph of host rock sample NM1721. (c) Hand specimen photograph of MME sample NM1722. (d) Photomicrograph of sample host rock 15TNM10-1; left: plane-polarized light (PPL); right: cross-polarized light (XPL). (e) Photomicrograph of MME sample 15TNM10-2; left: plane-polarized light (PPL); right: cross-polarized light (XPL). Mineral abbreviations: Q: quartz; Pl: plagioclase; Kfs: K-feldspar; Mt: magnetite; Amp: amphibole; Bt: biotite; Ap: apatite.

Figure 3. Representative CL images and U-Pb concordia diagrams of zircons. Small white circles show the locations of LA-ICP-MS U-Pb analysis spots. Large black dashed circles show the locations of corresponding Hf isotope analyses.

Figure 4. Histograms of $\varepsilon_{Hf}(t)$ values of zircons. (a) Host rock sample 15TNM10-1; (b) MME sample 15TNM10-2.

Figure 5. Amphibole chemistry of Nyemo pluton samples. (a) Cation occupancy of the B sites in the amphibole structural formula: B (Na) vs. B (Ca + Na) (after Leake et al., 1978). (b) Mg / (Mg + Fe^{2+}) vs. Si atoms per formula unit, with classification boundaries (after Leake et al., 1978). (c) Na_2O vs. SiO_2 (Coltorti et al., 2007). (d) TiO_2 vs. Al_2O_3 (wt%) (Jiang and An, 1984).

Figure 6. Whole-rock geochemistry diagrams. Data from previously published post-collisional adakitic rocks in Southern Tibet are plotted in some panels for comparison; reference data sources are listed in Table S4. (a) $Na_2O + K_2O$ vs. SiO_2 (after Middlemost, 1994). (b) A/NK vs. A/CNK, where A is Al_2O_3, C is CaO, K is K_2O, and N is Na_2O, all on a molar basis (after Maniar and Piccoli, 1989). (c) MgO vs. SiO_2; fields include thickened lower crust-derived adakites (after Muir, 1995; Petford and Atherton, 1996), subducted oceanic slab-derived adakites (Stern and Kilian, 1996 and references therein), high-SiO_2 adakites (HSA) and low SiO_2 adakites (LSA) (after Martin et al., 2005). (d) K_2O vs. SiO_2 (after Peccerillo and Taylor, 1976). (e) $\varepsilon_{Nd}(t)$ vs. SiO_2. (f) Sr/Y vs. SiO_2.

Figure 7. Trace element results. (a) Chondrite-normalized rare earth element patterns. (b) Primitive mantle-normalized extended trace element patterns of the Nyemo intrusive rocks. Chondrite values are from Boynton (1984). Primitive mantle values are from Sun and McDonough (1989). Himalayan sediment data are from Guo and

Wilson (2012); Yarlung MORB data are from Dai et al (2013); Upper crust and Lower crust data are from Taylor and McLennan (1985). (c) Discrimination of adakitic affinity: Sr/Y vs. Y (after Defant and Drummond, 1990). The black curves represent modeled batch partial melting trends with different starting materials and residual mineral assemblages. Reference data as in Fig. 6. The partition coefficients are from https://earthref.org/GERM/KDD/.

Figure 8. Isotopic data. (a) Sr and Nd isotope ratios of the Nyemo intrusive rocks in southern Tibet, corrected to average magmatic age of 28.5 Ma. (b) $^{207}Pb/^{204}Pb$ vs. $^{206}Pb/^{204}Pb$ (after Zhao et al., 2009). (c) $^{208}Pb/^{204}Pb$ vs. $^{206}Pb/^{204}Pb$ (after Zhao et al., 2009). (b) Percentage of mantle-derived Hf in zircons for Tibetan adakite-like magmatic rocks, plotted as a function of zircon U-Pb age (modified from Zhu et al., 2011). Reference data as in Fig. 6.

Figure 9. Indications of magma mixing. (a) FeO^T vs. MgO (after Zorpi et al., 1989). (b)1/V vs. Rb/V with schematic diagram, where curves showing melt compositions produced by fractional crystallization and partial melting processes and the line indicating a simple linear regression line (after Schiano et al., 2010).

Figure 10. (a) K_2O versus Na_2O (after Wang et al., 2012). (b) Th/Yb versus Ta/Yb diagram (Pearce, 1983). The average compositions for N-MORB and for continental lithospheric mantle are from Sun and McDonough (1989). (c) $^{143}Nd/^{144}Nd$ vs. Rb/Sr (after Liu et al., 2017). (d) Rb/Y vs. Nb/Y. (e) Variations in Rb/Sr vs. Ba/Rb that may constrain source mineralogy. The data suggest minor amounts of both amphibole and phlogopite (Furman and Graham, 1999). (f) Rb vs. Cr; black points mark increments

of increasing percentage of batch modal melting of a mafic source, in this case a mantle xenolith of phlogopite–garnet clinopyroxenite with 21 ppm Rb, 562 ppm Cr, and mineral modes 0.50 clinopyroxene, 0.45 garnet and 0.05 phlogopite. Mineral/melt partition coefficients are from (Jiang et al., 2006). Reference data as in Fig. 6.

Figure 11. (a) Na_2O vs. CMF (molar CaO / (MgO + FeO^T). Outlined regions from Altherr and Siebel (2002) and Patiño Douce (1999). Abreviations: MB: meta-basalts; MA: meta-andesites; MGW: metagreywackes; MP: metapelites. (b) Trace element plots of Ba/Nb vs. La/Nb. The compositions of different end members in (b) are after Wilson (2001).

Figure 12. Plots of La/Yb ratios vs. magmatic ages for the post-collisional high Sr/Y rocks with adakitic affinity (modified from Chung et al., 2009). Reference data as in Fig. 6.

Declaration of interests

☒ The authors declare that they have no known competing financial interests or personal relationships that could have appeared to influence the work reported in this paper.

☐The authors declare the following financial interests/personal relationships which may be considered as potential competing interests:

Table 1

Host rocks		15TNM10-1	NM1714	NM1715	NM1717	NM1720	NM1721	**MMEs**		15TNM10-2	NM1716	NM1718	NM1719	NM1722
	SiO_2	66.11	65.93	66.19	63.28	66.93	65.25		SiO_2	55.60	56.61	53.87	52.91	52.96
	TiO_2	0.63	0.70	0.62	0.63	0.61	0.62		TiO_2	1.27	1.21	1.35	1.44	1.41
	Al_2O_3	15.58	15.96	15.86	14.85	15.36	15.93		Al_2O_3	17.71	17.28	17.88	18.09	18.45
	TFe_2O_3	3.73	3.83	3.80	3.82	3.64	3.81		TFe_2O_3	6.87	6.77	7.71	8.07	8.03
	MnO	0.05	0.05	0.05	0.05	0.05	0.05		MnO	0.11	0.09	0.12	0.13	0.12
	MgO	1.25	1.38	1.33	1.26	1.28	1.41		MgO	2.74	2.64	3.22	3.36	3.25
	CaO	2.88	3.25	3.02	2.84	2.83	3.09		CaO	5.20	4.82	5.43	5.61	5.55
	Na_2O	4.11	4.61	4.24	4.13	4.01	4.12		Na_2O	4.38	4.26	4.57	4.65	4.87
	K_2O	4.15	2.76	3.87	3.42	4.21	4.31		K_2O	4.53	4.52	3.91	3.57	3.62
	P_2O_5	0.29	0.32	0.29	0.27	0.29	0.28		P_2O_5	0.62	0.65	0.72	0.78	0.69

LOI	0.67	0.52	0.47	0.40	0.33	0.49	LOI	0.78	0.43	0.55	0.95	0.42
Li	31.0	35.7	25.1	29.2	29.5	34.5	Li	46.4	42.4	53.9	56.8	58.5
Be	3.07	3.27	2.96	2.85	2.69	3.39	Be	3.84	3.47	4.35	4.92	4.28
Sc	4.42	5.38	4.97	3.99	4.51	5.97	Sc	13.2	9.13	15.1	14.5	12.3
V	64.5	81.6	67.9	73.5	68.0	70.4	V	139	137	145	157	156
Cr	8.59	10.7	8.54	13.2	11.6	13.2	Cr	27.5	25.6	35.7	43.2	28.4
Co	7.34	9.58	8.44	8.90	8.42	9.19	Co	16.1	18.0	19.3	21.4	20.6
Ni	8.28	9.53	8.53	10.6	10.2	11.4	Ni	19.5	18.5	25.7	29.7	22.5
Cu	14.5	67.2	50.1	38.5	23.1	33.2	Cu	108	119	75.1	89.9	72.2
Zn	70.8	77.5	73.8	71.2	67.4	71.6	Zn	140	116	140	147	142
Ga	21.4	23.9	22.1	20.7	21.6	22.0	Ga	25.9	25.1	27.1	28.4	28.2
Rb	147	133	142	139	151	164	Rb	163	179	171	185	185
Sr	696	702	753	778	745	757	Sr	816	915	806	774	818
Y	8.75	10.8	9.27	9.12	8.89	9.98	Y	16.5	13.2	17.1	18.6	18.5
Zr	221	227	210	186	216	188	Zr	342	285	275	335	317
Nb	16.6	15.9	13.8	13.8	13.7	16.0	Nb	36.2	23.7	33.2	37.3	43.3
Sn	2.12	2.20	1.92	1.74	1.80	1.91	Sn	4.68	3.18	4.15	4.68	4.27
Cs	7.33	5.59	6.96	5.31	5.82	8.08	Cs	7.68	7.04	8.96	11.4	9.54
Ba	1017	607	1104	845	1011	1067	Ba	967	1127	890	714	835
La	50.7	76.4	53.4	56.8	68.7	66.5	La	71.1	83.6	96.1	92.8	133
Ce	106	138	102	106	120	122	Ce	186	175	205	214	252
Pr	13.1	14.4	11.2	11.8	12.8	13.2	Pr	24.6	19.6	23.7	25.7	27.0

Nd	43.4	50.2	40.5	42.8	44.1	45.7	Nd	93.5	71.1	86.4	94.5	93.9
Sm	6.64	7.45	6.29	6.43	6.43	6.65	Sm	12.4	10.4	13.1	14.2	12.9
Eu	1.39	1.47	1.35	1.36	1.31	1.37	Eu	2.66	2.41	2.59	3.02	2.73
Gd	3.81	3.90	3.44	3.33	3.33	3.36	Gd	7.31	5.34	7.19	7.61	7.04
Tb	0.43	0.47	0.38	0.41	0.40	0.42	Tb	0.81	0.66	0.78	0.86	0.84
Dy	2.02	2.16	1.94	1.90	1.82	2.03	Dy	3.69	2.91	3.75	3.91	3.84
Ho	0.32	0.36	0.30	0.32	0.29	0.33	Ho	0.57	0.45	0.60	0.65	0.63
Er	0.82	1.08	0.95	0.91	0.88	0.93	Er	1.38	1.28	1.74	1.83	1.92
Tm	0.11	0.12	0.11	0.10	0.10	0.11	Tm	0.18	0.15	0.18	0.20	0.20
Yb	0.68	0.79	0.62	0.67	0.63	0.68	Yb	1.06	0.87	1.16	1.28	1.25
Lu	0.098	0.11	0.10	0.0098	0.093	0.095	Lu	0.15	0.12	0.17	0.19	0.18
Hf	5.85	5.83	5.16	4.47	5.13	4.63	Hf	8.81	6.74	7.02	8.20	7.78
Ta	1.25	1.28	1.08	1.03	1.05	1.29	Ta	2.53	1.46	2.57	2.76	3.29
Tl	1.01	1.12	1.16	1.19	1.24	1.36	Tl	1.11	1.57	1.48	1.65	1.68
Pb	51.0	36.0	45.9	48.0	50.6	57.0	Pb	57.4	57.8	48.1	51.1	48.5
Th	28.6	28.2	23.4	18.8	37.7	34.3	Th	29.8	26.1	33.8	40.3	41.2
U	5.84	5.47	5.00	3.59	6.21	6.42	U	5.12	4.12	5.90	6.48	4.78
$^{143}Nd/^{144}Nd$	0.512486			0.512505	0.512499	0.512473	$^{143}Nd/^{144}Nd$	0.512443	0.512464	0.512466	0.512438	
1sigma	0.000005			0.000006	0.000005	0.000005	1sigma	0.000004	0.000005	0.000005	0.000005	
$^{87}Sr/^{86}Sr$	0.706852			0.706	0.706	0.707	$^{87}Sr/^{86}Sr$	0.706859	0.706	0.706	0.706	

r		78	76	01	r	91	88	99
		9	3	1		2	9	2
		0.0	0.0	0.0		0.0	0.0	0.0
		00	00	00		00	00	00
1sig	0.00	00	00	00	1sig	0.00	00	00	00
ma	0004	7	7	7	ma	0008	6	5	6
^{206}P		18.	18.	18.	^{206}P		18.	18.	18.
b/^{20}	18.5	49	49	49	b/^{20}	18.4	49	50	50
^{4}Pb	103	44	99	80	^{4}Pb	971	15	43	34
		0.0	0.0	0.0			0.0	0.0	0.0
1sig	0.00	00	00	00	1sig	0.00	00	00	00
ma	04	4	4	5	ma	03	5	5	6
^{207}P		15.	15.	15.	^{207}P		15.	15.	15.
b/^{20}	15.6	68	67	68	b/^{20}	15.6	68	68	68
^{4}Pb	812	11	90	19	^{4}Pb	814	24	12	29
		0.0	0.0	0.0			0.0	0.0	0.0
1sig	0.00	00	00	00	1sig	0.00	00	00	00
ma	04	4	4	4	ma	03	4	4	5
^{208}P		38.	38.	38.	^{208}P		38.	38.	38.
b/^{20}	38.9	93	95	94	b/^{20}	38.9	94	96	96
^{4}Pb	472	91	08	64	^{4}Pb	449	66	56	67
		0.0	0.0	0.0			0.0	0.0	0.0
1sig	0.00	01	01	01	1sig	0.00	01	01	01
ma	10	1	0	1	ma	08	2	1	3
		2.1	2.1	2.1			2.1	2.1	2.1
^{208}P		05	05	05	^{208}P		06	05	05
b/^{20}	2.10	45	45	44	b/^{20}	2.10	18	76	92
^{6}Pb	4080	8	8	2	^{6}Pb	5468	7	4	3
		0.0	0.0	0.0			0.0	0.0	0.0
		00	00	00			00	00	00
1sig	0.00	01	01	01	1sig	0.00	01	01	01
ma	0018	8	8	7	ma	0015	8	9	9
		0.8	0.8	0.8			0.8	0.8	0.8
^{207}P		47	47	47	^{207}P		48	47	47
b/^{20}	0.84	88	52	76	b/^{20}	0.84	08	44	57
^{6}Pb	7158	5	0	1	^{6}Pb	7781	7	0	1
		0.0	0.0	0.0			0.0	0.0	0.0
		00	00	00			00	00	00
1sig	0.00	00	00	00	1sig	0.00	00	00	00
ma	0005	5	5	5	ma	0004	5	5	6

- High Sr/Y host rocks of Nyemo pluton are derived from thickened lower crust
- Coeval shoshonitic enclaves were produced from enriched lithospheric mantle
- Lithospheric mantle convective removal, onsets of extension may have occurred during Oligocene

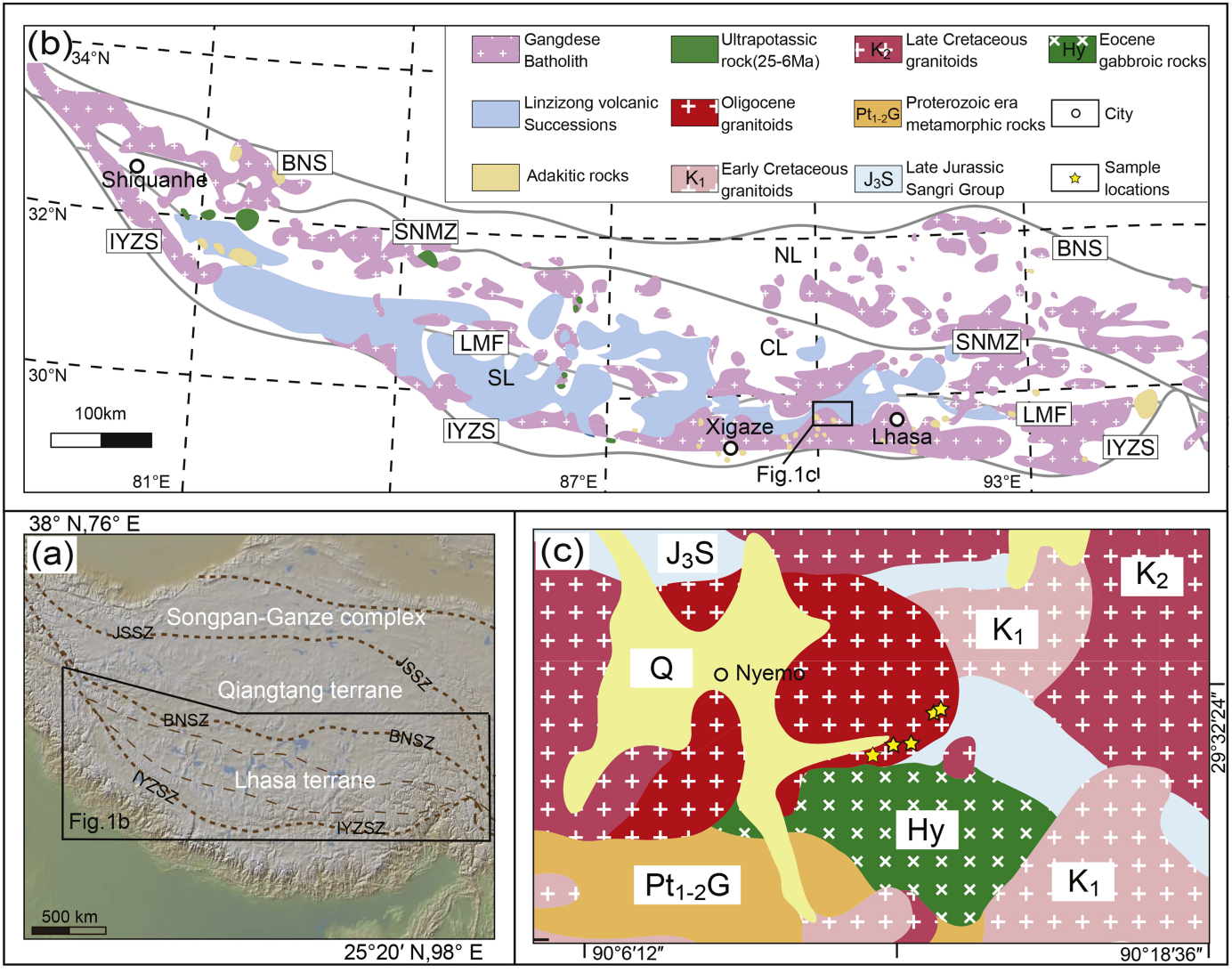
(b)
34°N
32°N
30°N
81°E
87°E
93°E
100km
Shiquanhe
BNS
IYZS
SNMZ
NL
LMF
SL
CL
Xigaze
Lhasa
Fig.1c
Gangdese Batholith
Ultrapotassic rock(25-6Ma)
Late Cretaceous granitoids
Eocene gabbroic rocks
Linzizong volcanic Successions
Oligocene granitoids
Proterozoic era metamorphic rocks
City
Adakitic rocks
Early Cretaceous granitoids
Late Jurassic Sangri Group
Sample locations
38° N,76° E
(a)
Songpan-Ganze complex
JSSZ
Qiangtang terrane
BNSZ
Lhasa terrane
IYZSZ
Fig.1b
500 km
25°20′ N,98° E
(c)
Q
Nyemo
Hy
29°32′24″
90°6′12″
90°18′36″

Figure 1

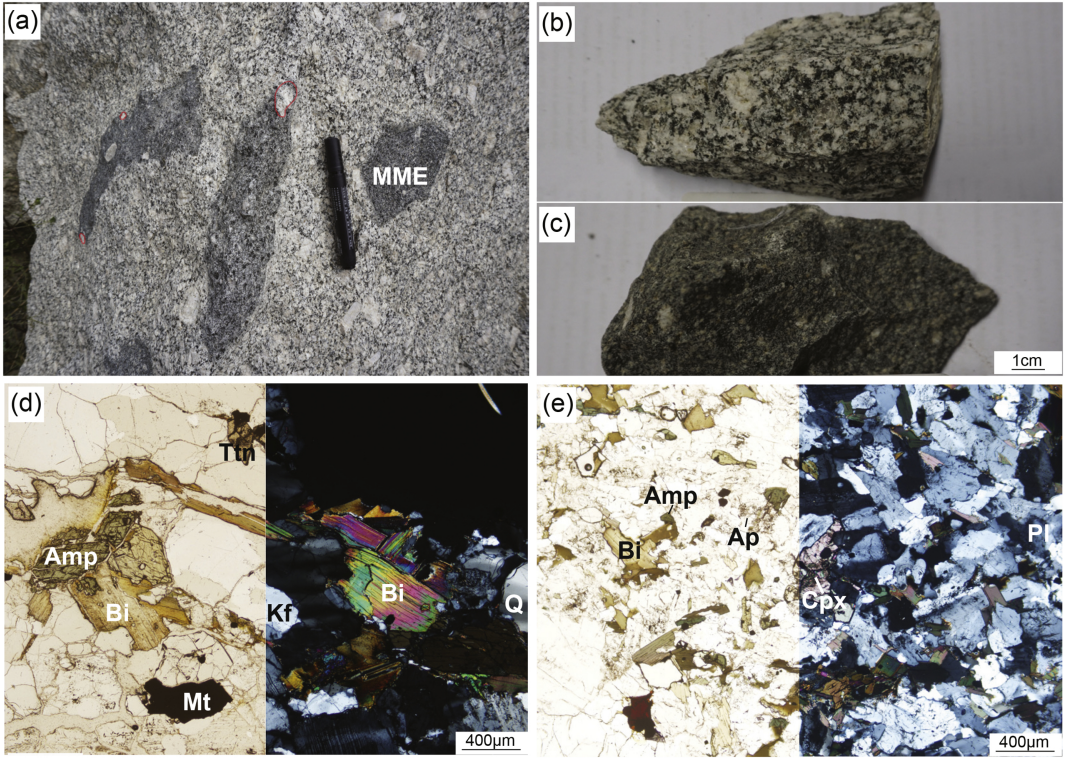

Figure 2

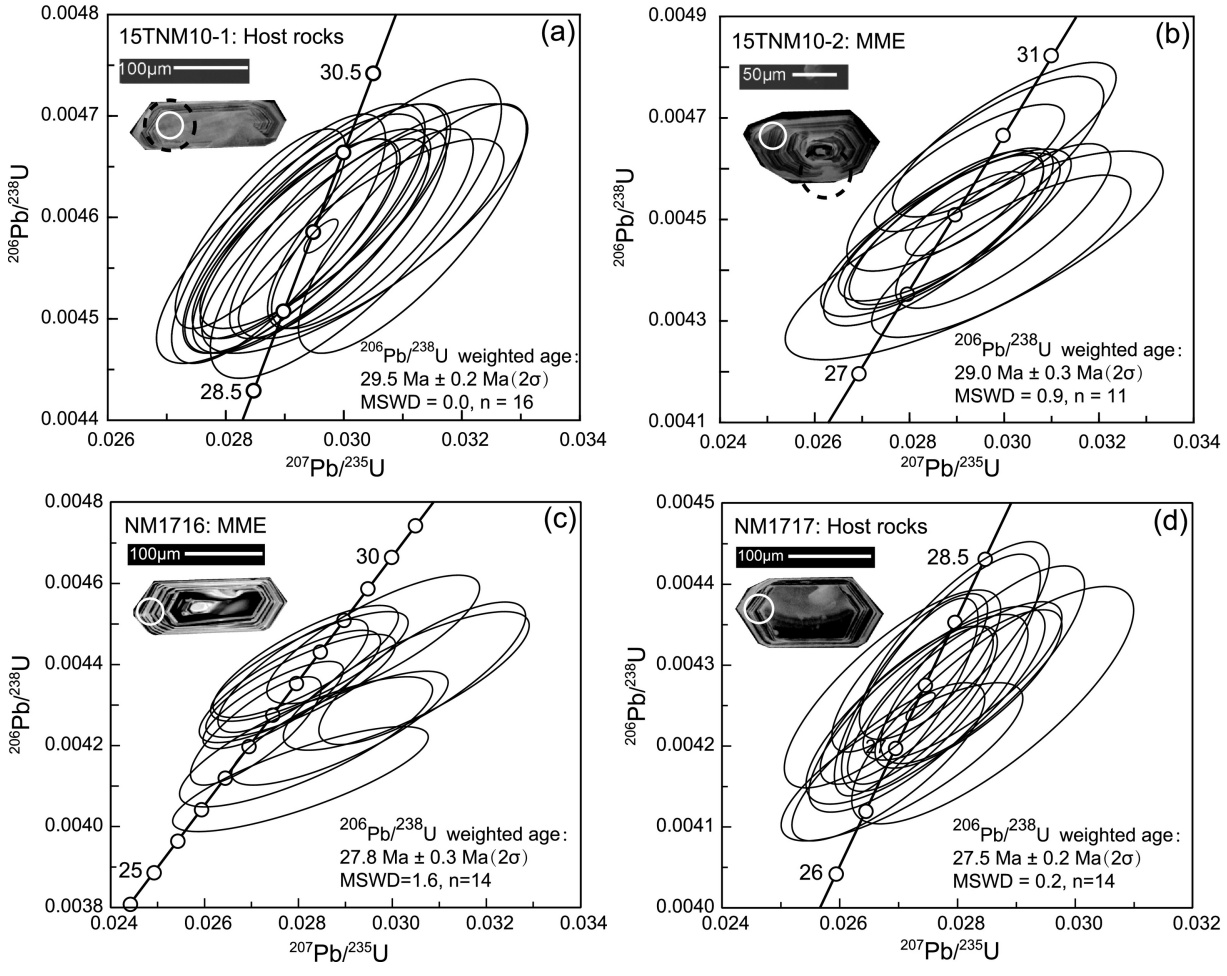
15TNM10-1: Host rocks
(a)
100μm
30.5
28.5
$^{206}Pb/^{238}U$ weighted age:
29.5 Ma ± 0.2 Ma(2σ)
MSWD = 0.0, n = 16
15TNM10-2: MME
(b)
50μm
31
27
$^{206}Pb/^{238}U$ weighted age:
29.0 Ma ± 0.3 Ma(2σ)
MSWD = 0.9, n = 11
NM1716: MME
(c)
100μm
30
25
$^{206}Pb/^{238}U$ weighted age:
27.8 Ma ± 0.3 Ma(2σ)
MSWD=1.6, n=14
NM1717: Host rocks
(d)
100μm
28.5
26
$^{206}Pb/^{238}U$ weighted age:
27.5 Ma ± 0.2 Ma(2σ)
MSWD = 0.2, n=14
$^{206}Pb/^{238}U$
$^{207}Pb/^{235}U$

Figure 3

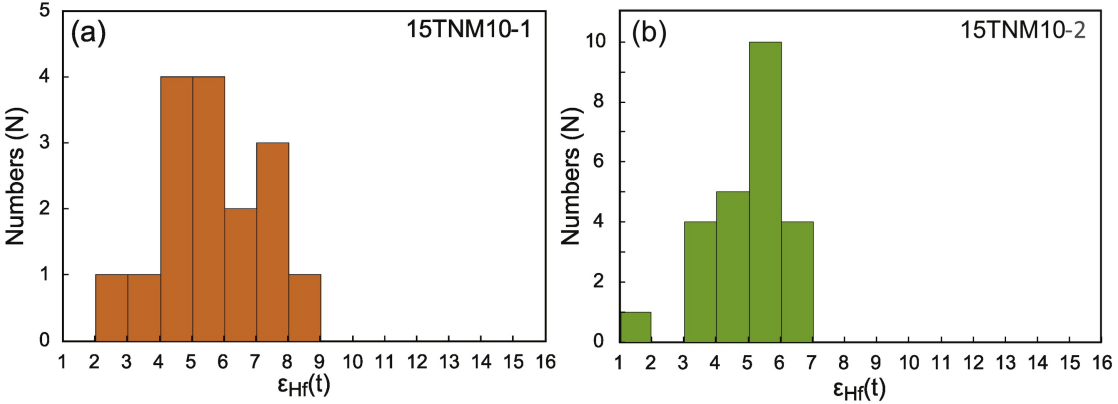

Figure 4

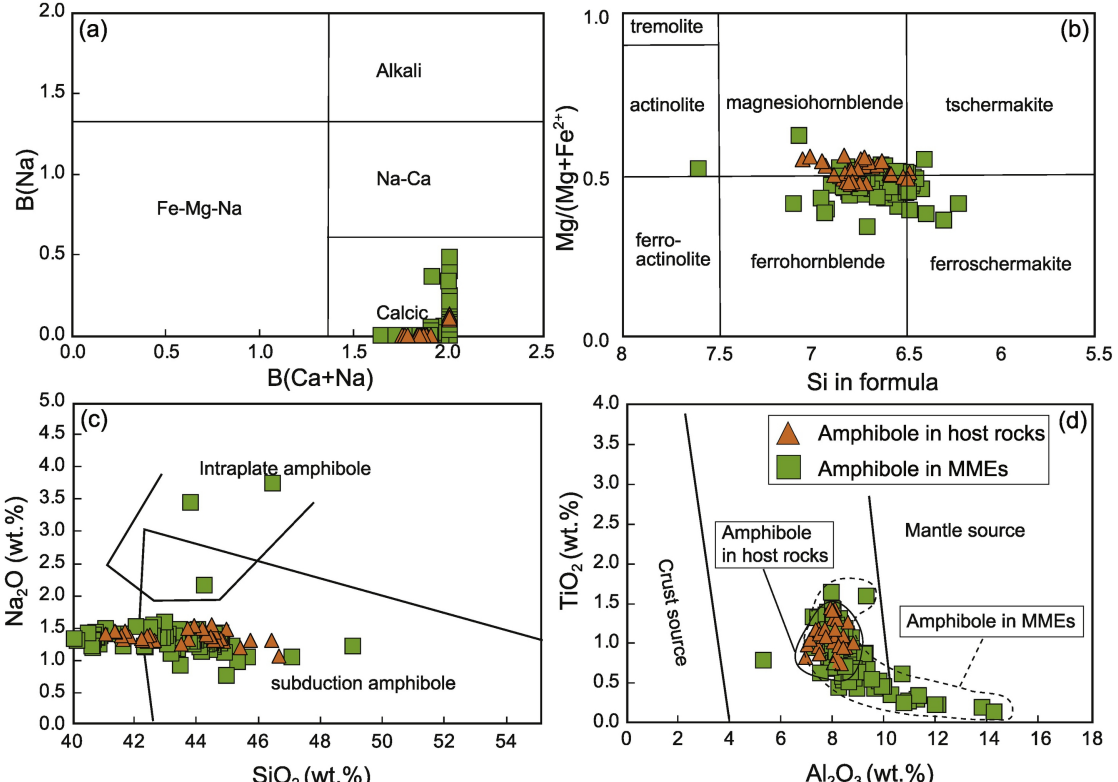
(a)
Alkali
Na-Ca
Fe-Mg-Na
Calcic
B(Na)
B(Ca+Na)
(b)
tremolite
actinolite
magnesiohornblende
tschermakite
ferro-
actinolite
ferrohornblende
ferroschermakite
Mg/(Mg+Fe2+)
Si in formula
(c)
Intraplate amphibole
subduction amphibole
Na2O (wt.%)
SiO2 (wt.%)
(d)
Amphibole in host rocks
Amphibole in MMEs
Amphibole
in host rocks
Mantle source
Crust source
Amphibole in MMEs
TiO2 (wt.%)
Al2O3 (wt.%)

Figure 5

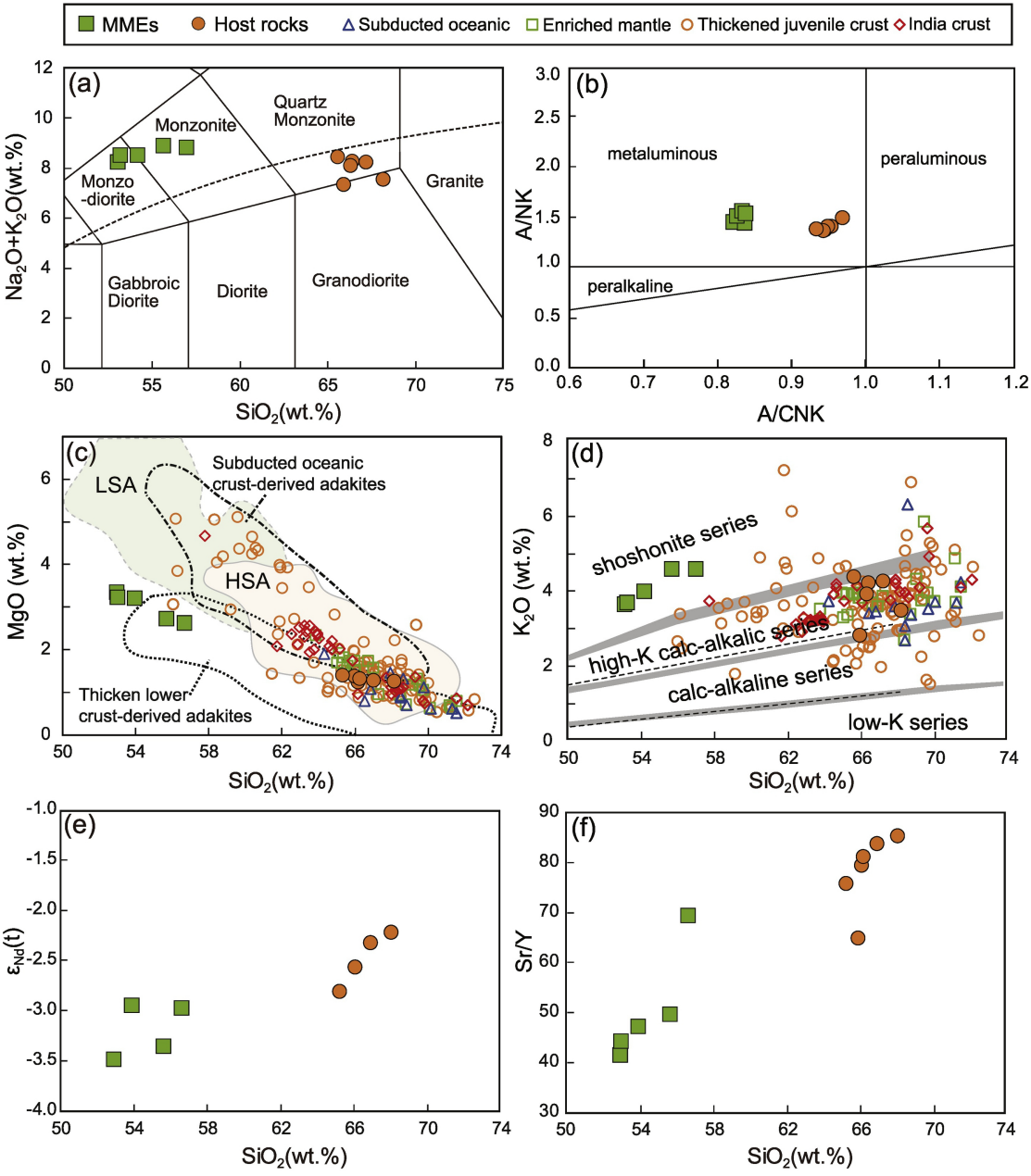
MMEs
Host rocks
Subducted oceanic
Enriched mantle
Thickened juvenile crust
India crust
(a)
Monzonite
Quartz Monzonite
Monzo -diorite
Granite
Gabbroic Diorite
Diorite
Granodiorite
Na2O+K2O(wt.%)
SiO2(wt.%)
(b)
metaluminous
peraluminous
peralkaline
A/NK
A/CNK
(c)
LSA
Subducted oceanic crust-derived adakites
HSA
Thicken lower crust-derived adakites
MgO (wt.%)
SiO2(wt.%)
(d)
shoshonite series
high-K calc-alkalic series
calc-alkaline series
low-K series
K2O (wt.%)
SiO2(wt.%)
(e)
εNd(t)
SiO2(wt.%)
(f)
Sr/Y
SiO2(wt.%)

Figure 6

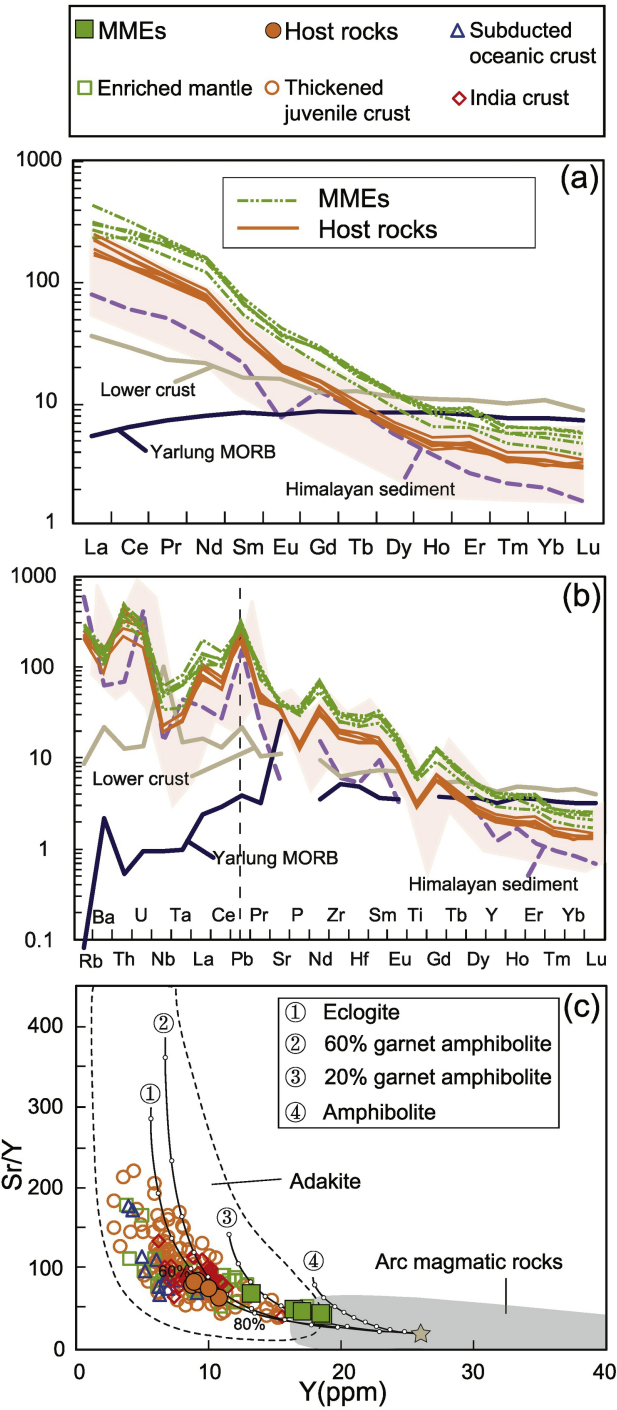
MMEs
Host rocks
Subducted oceanic crust
Enriched mantle
Thickened juvenile crust
India crust
(a)
MMEs
Host rocks
Lower crust
Yarlung MORB
Himalayan sediment
1000
100
10
1
La Ce Pr Nd Sm Eu Gd Tb Dy Ho Er Tm Yb Lu
(b)
Lower crust
Yarlung MORB
Himalayan sediment
1000
100
10
1
0.1
Rb Th Nb La Ce Pr P Zr Sm Ti Tb Y Er Yb
Ba U Ta Pb Sr Nd Hf Eu Gd Dy Ho Tm Lu
(c)
① Eclogite
② 60% garnet amphibolite
③ 20% garnet amphibolite
④ Amphibolite
Adakite
Arc magmatic rocks
60%
80%
Sr/Y
Y(ppm)
400
300
200
100
0
10
20
30
40

Figure 7

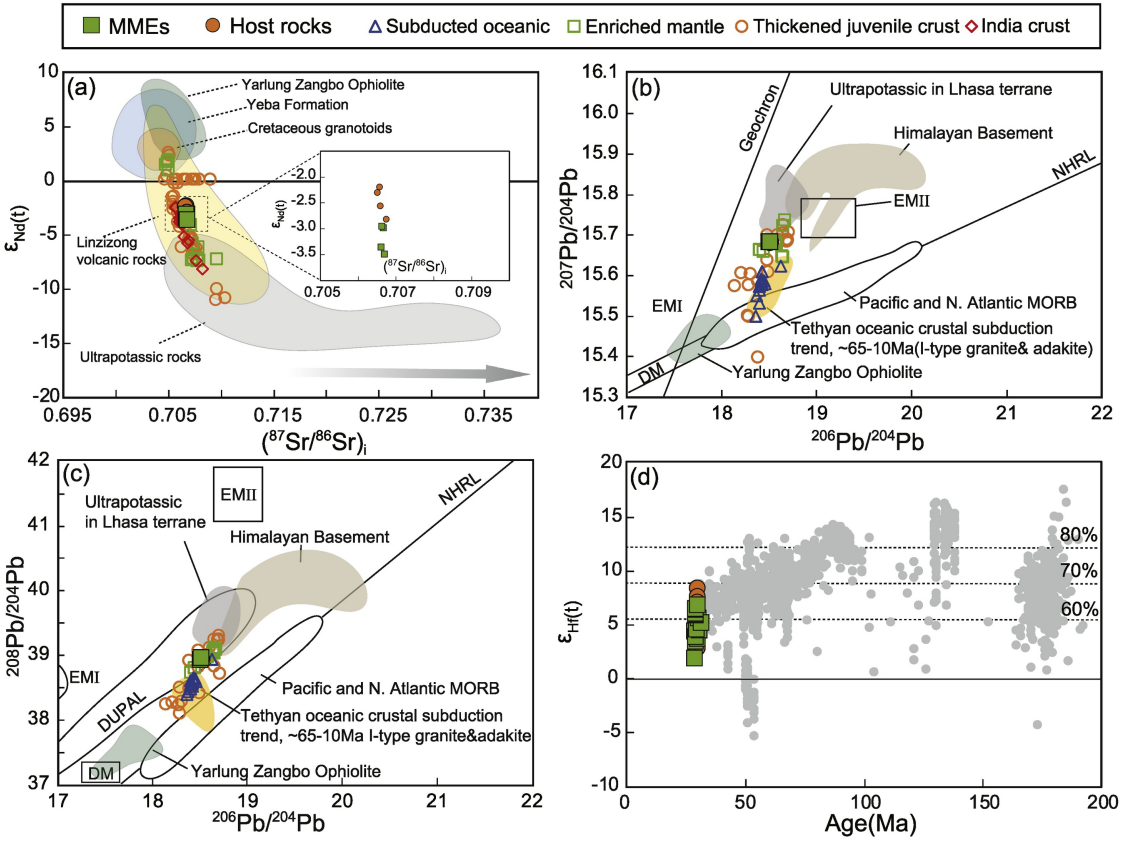
MMEs
Host rocks
Subducted oceanic
Enriched mantle
Thickened juvenile crust
India crust
(a)
Yarlung Zangbo Ophiolite
Yeba Formation
Cretaceous granotoids
Linzizong volcanic rocks
Ultrapotassic rocks
εNd(t)
(87Sr/86Sr)i
(b)
Geochron
Ultrapotassic in Lhasa terrane
Himalayan Basement
NHRL
EMII
EMI
DM
Pacific and N. Atlantic MORB
Tethyan oceanic crustal subduction trend, ~65-10Ma(I-type granite& adakite)
Yarlung Zangbo Ophiolite
207Pb/204Pb
206Pb/204Pb
(c)
Ultrapotassic in Lhasa terrane
EMII
NHRL
Himalayan Basement
EMI
DUPAL
Pacific and N. Atlantic MORB
Tethyan oceanic crustal subduction trend, ~65-10Ma I-type granite&adakite
DM
Yarlung Zangbo Ophiolite
208Pb/204Pb
206Pb/204Pb
(d)
80%
70%
60%
εHf(t)
Age(Ma)

Figure 8

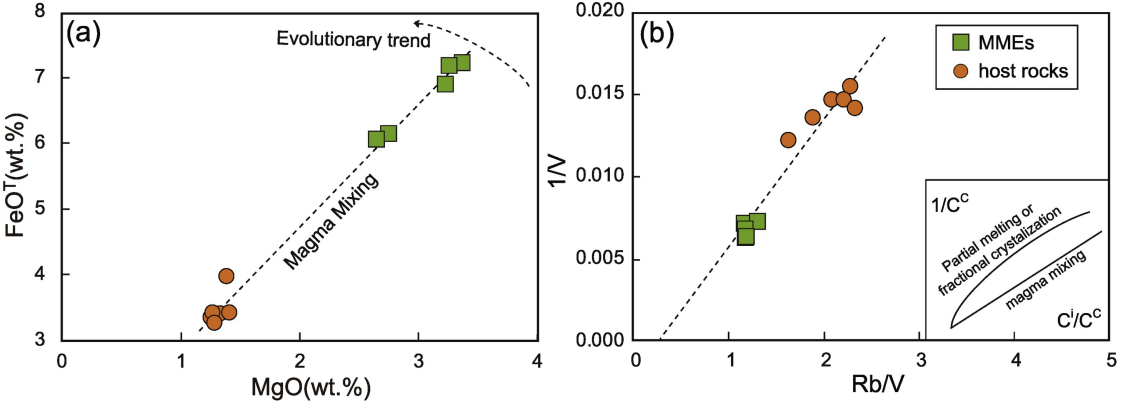
(a)
Evolutionary trend
Magma Mixing
FeO^T(wt.%)
MgO(wt.%)
(b)
MMEs
host rocks
1/V
Rb/V
1/C^C
Partial melting or fractional crystalization
magma mixing
C^i/C^C

Figure 9

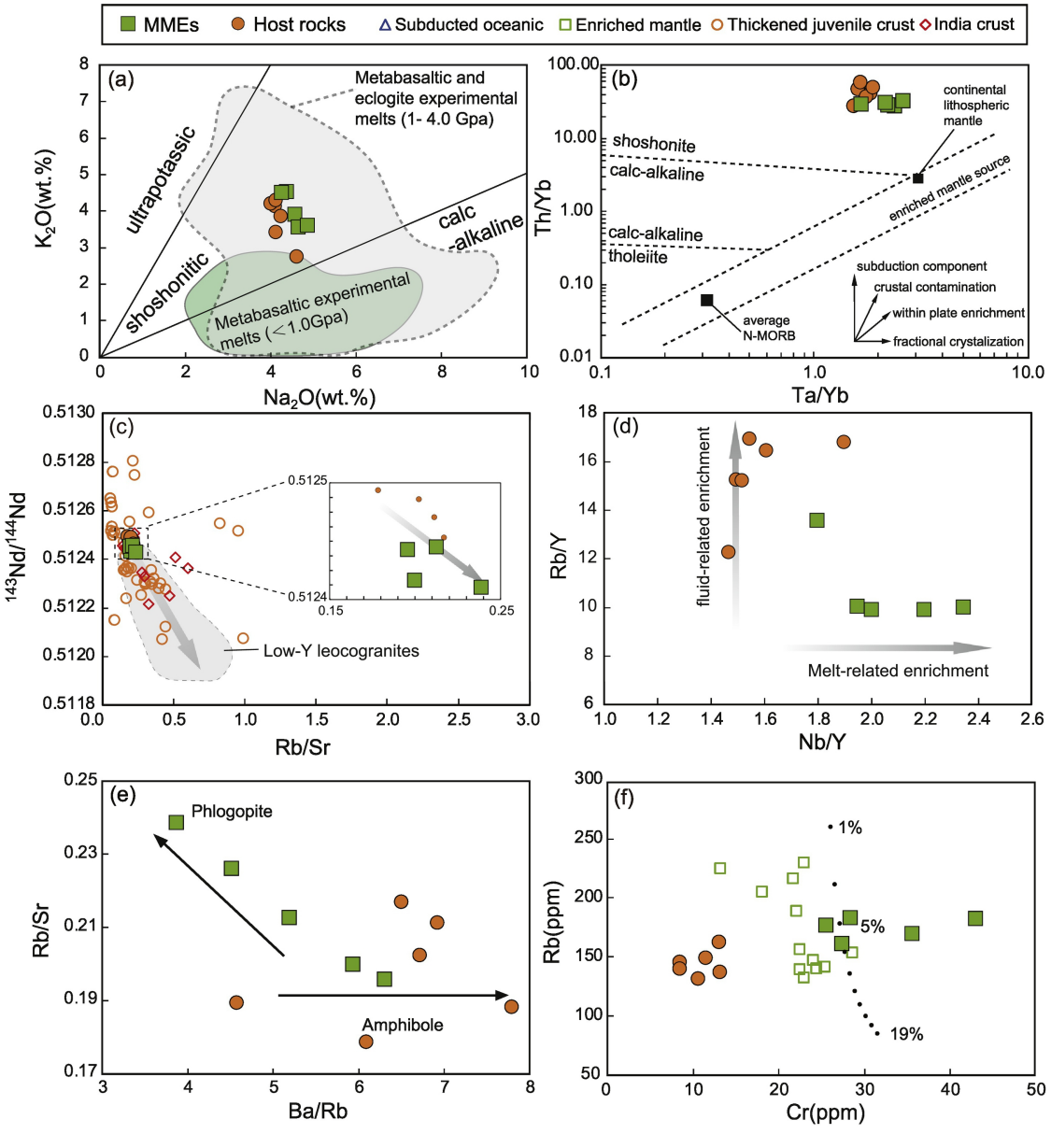
MMEs
Host rocks
Subducted oceanic
Enriched mantle
Thickened juvenile crust
India crust
(a)
Metabasaltic and eclogite experimental melts (1- 4.0 Gpa)
ultrapotassic
shoshonitic
calc -alkaline
Metabasaltic experimental melts (<1.0Gpa)
K2O(wt.%)
Na2O(wt.%)
(b)
continental lithospheric mantle
shoshonite
calc-alkaline
calc-alkaline
tholeiite
enriched mantle source
subduction component
crustal contamination
within plate enrichment
fractional crystalization
average N-MORB
Th/Yb
Ta/Yb
(c)
Low-Y leocogranites
143Nd/144Nd
Rb/Sr
(d)
fluid-related enrichment
Melt-related enrichment
Rb/Y
Nb/Y
(e)
Phlogopite
Amphibole
Rb/Sr
Ba/Rb
(f)
1%
5%
19%
Rb(ppm)
Cr(ppm)

Figure 10

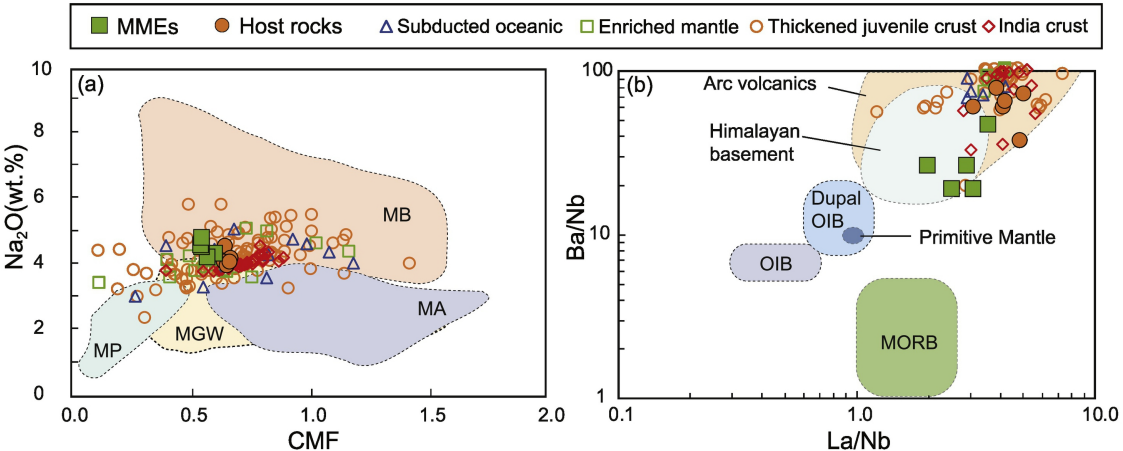
MMEs
Host rocks
Subducted oceanic
Enriched mantle
Thickened juvenile crust
India crust
(a)
Na2O(wt.%)
CMF
MB
MA
MGW
MP
(b)
Ba/Nb
La/Nb
Arc volcanics
Himalayan basement
Dupal OIB
Primitive Mantle
OIB
MORB

Figure 11

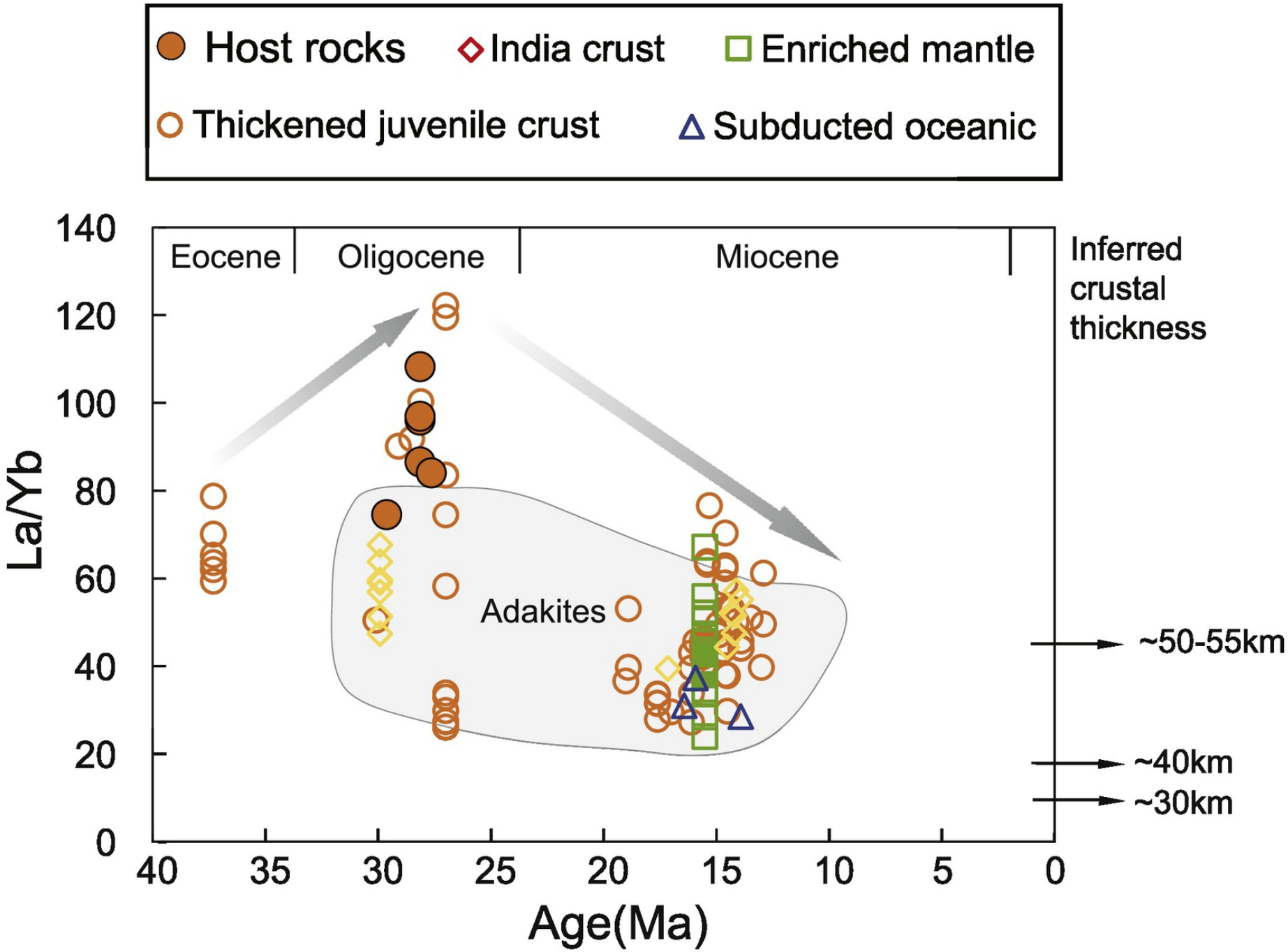
Host rocks
India crust
Enriched mantle
Thickened juvenile crust
Subducted oceanic
Eocene
Oligocene
Miocene
Inferred crustal thickness
Adakites
~50-55km
~40km
~30km
La/Yb
Age(Ma)
0
20
40
60
80
100
120
140
40
35
30
25
20
15
10
5
0

Figure 12